Downloaded from rsta.royalsocietypublishing.org

PHILOSOPHICAL TRANSACTIONS OF THE ROYAL SOCIETY A MATHEMATICAL, PHYSICAL & ENGINEERING SCIENCES

The Elliptic Umbilic Diffraction Catastrophe

M. V. Berry, J. F. Nye and F. J. Wright

Phil. Trans. R. Soc. Lond. A 1979 **291**, 453-484
doi: 10.1098/rsta.1979.0039

Email alerting service

Receive free email alerts when new articles cite this article - sign up in the box at the top right-hand corner of the article or click **here**

To subscribe to *Phil. Trans. R. Soc. Lond. A* go to: **http://rsta.royalsocietypublishing.org/subscriptions**

This journal is © 1979 The Royal Society

Downloaded from rsta.royalsocietypublishing.org

THE ELLIPTIC UMBILIC DIFFRACTION CATASTROPHE

By M. V. BERRY, J. F. NYE, F.R.S. and F. J. WRIGHT
H. H. Wills Physics Laboratory, University of Bristol, Tyndall Avenue, Bristol BS8 1TL, U.K.

(*Received* 19 *July* 1978)

[Plates 1–4]

CONTENTS

We have made a detailed theoretical and experimental study of the three-dimensional diffraction pattern decorating the geometrical-optics caustic surface whose form is the elliptic umbilic catastrophe in Thom's classification. This caustic has three sheets joined along three parabolic cusped edges ('ribs') which touch at one singular point (the 'focus').

Experimentally, the diffraction catastrophe was studied in light refracted by a water droplet 'lens' with triangular perimeter, and photographed in sections perpendicular to the symmetry axis of the pattern. Theoretically, the pattern was represented by a diffraction integral $E(x, y, z)$, which was studied numerically through computer simulations and analytically by the method of stationary phase. Particular attention was concentrated on the 'dislocation lines' where $|E|$ vanishes, since these can be considered as a skeleton on which the whole diffraction pattern is built.

Within the region bounded by the caustic surface the interference of four rays produces hexagonal diffraction maxima stacked in space like the atoms of a distorted crystal with space group $R\bar{3}m$. The dislocation lines not too close to the ribs form hexagonally puckered rings. On receding from the focus and approaching the ribs, these rings approach one another and eventually join to form 'hairpins', each arm of which is a tightly wound sheared helix that develops asymptotically into one of the dislocations of the cusp diffraction catastrophe previously studied by Pearcey.

Outside the caustic there are also helical dislocation lines, this time formed by interference involving a complex ray.

There is close agreement, down to the finest details, between observation, exact computation of $E(x, y, z)$, and the four-wave stationary-phase approximation.

Vol. 291. A 1382. 32 [Published 12 April 1979

The Royal Society is collaborating with JSTOR to digitize, preserve, and extend access to *Philosophical Transactions of the Royal Society of London. Series A, Mathematical and Physical Sciences.* www.jstor.org

Downloaded from rsta.royalsocietypublishing.org

1. Introduction

The classification by Thom (1975) of singularities of gradient mappings as 'elementary catastrophes' is directly applicable to the focusing of rays or trajectories in optics and quantum mechanics, in that it gives a description of the caustic surfaces enveloped by families of rays (Berry 1976; Berry & Nye 1977; Nye 1978; Poston & Stewart 1978). If a caustic is to be stable under perturbation its local structure must conform to that of one of the catastrophes. In three-dimensional space this restricts stable caustics to smooth 'fold' surfaces, which may have line singularities in the form of cusped edges ('ribs'), and the ribs may themselves have point singularities described by the swallowtail, hyperbolic umbilic or elliptic umbilic catastrophes. However, the application of catastrophe theory to caustics goes deeper than a mere listing of their possible forms: it also provides an explanation of the characteristic diffraction pattern associated with each catastrophe. These patterns arise from the finite wavelength of light or the finite value of Planck's constant (Duistermaat 1974; Arnol'd 1975; Berry 1976); Trinkaus & Drepper (1977) have felicitously termed them 'diffraction catastrophes'. The diffraction pattern decorating the focus of a perfect lens (Linfoot & Wolf 1956*a*, *b*; Boivin & Wolf 1965; Boivin, Dow & Wolf 1967) is not a diffraction catastrophe, because the focus itself is not a catastrophe: it is an isolated point in space and is unstable against perturbation.

The diffraction catastrophes form a hierarchy, each member of which is described by a complex wavefunction $G(x, y, z, \ldots)$ giving the dependence of the diffraction on 'control parameters' $x, y, z, \ldots$ (which could represent, say, coordinates of a point in space). Each wavefunction has the form of a diffraction integral:

$$G(x, y, z, \ldots) = \frac{1}{2\pi}\int_{-\infty}^{\infty} \mathrm{d}\xi \int_{-\infty}^{\infty} \mathrm{d}\eta \exp\left[\mathrm{i}P(\xi, \eta; x, y, z, \ldots)\right], \tag{1.1}$$

where in the exponent P is one of the 'potentials', depending on 'state variables' ξ, η as well as the control parameters, in Thom's list of standard forms describing the different catastrophes. Only the first member of the hierarchy of functions G can be expressed in terms of the standard 'special functions' of analysis; this corresponds to the fold catastrophe, for which G is the Airy function, first studied by Airy (1838), which can be written as a sum of two Bessel functions (Abramowitz & Stegun 1964, p. 446). The next diffraction catastrophe, corresponding to the cusp, was studied by Pearcey (1946), who computed contours of the modulus and phase of G.

It is our purpose here to present the results of a detailed experimental and theoretical study of the diffraction catastrophe corresponding to Thom's elliptic umbilic singularity. It involves two state variables and three control parameters, and has the potential function

$$P(\xi, \eta; x, y, z) = \xi^3 - 3\xi\eta^2 - z(\xi^2 + \eta^2) - x\xi - y\eta. \tag{1.2}$$

For fixed controls x, y, z the condition that P should be stationary determines ξ, η. Thus, we have the following gradient mapping:

$$\partial P/\partial\xi = 3(\xi^2 - \eta^2) - 2z\xi - x = 0; \quad \partial P/\partial\eta = -6\xi\eta - 2z\eta - y = 0. \tag{1.3}$$

In optics the solutions (ξ, η) of these equations give the points on an initial wavefront whose normals (rays) pass through (x, y, z). The caustic surface in (x, y, z) is defined by the singularities of this mapping, that is, by the additional condition that the solutions of (1.3) are degenerate, so that the gradient of P has a zero of order higher than unity. This requires the vanishing of the Hessian determinant of P, namely

$$(\partial^2 P/\partial\xi^2)\,(\partial^2 P/\partial\eta^2) - (\partial^2 P/\partial\xi\,\partial\eta)^2 = 0. \tag{1.4}$$

Downloaded from rsta.royalsocietypublishing.org

In terms of a parameter ϕ varying from 0 to 2π (1.3) and (1.4) give, for the equation of the caustic,

$$\left.\begin{aligned} x &= \tfrac{1}{3}z^2(\cos 2\phi - 2\cos\phi), \\ y &= -\tfrac{1}{3}z^2(\sin 2\phi + 2\sin\phi). \end{aligned}\right\} \tag{1.5}$$

For fixed z (1.5) describes a hypocycloid with three cusps. In space there are three sheets (figure 1) joined along three parabolic ribs that touch at the singular point $x = y = z = 0$, which we call the 'focus'. The ribs have the equations

$$r = z^2, \quad \theta = 0, \tfrac{2}{3}\pi, \tfrac{4}{3}\pi, \tag{1.6}$$

where r and θ are polar coordinates corresponding to x, y. At each point inside the region bounded by the three caustic sheets the gradient mapping (1.3) has four solutions (ξ, η) – that is, there are four rays through each point – while at points outside the caustic there are only two solutions (ξ, η). The diffraction function $G(x, y, z)$, which we now denote by $E(x, y, z)$ and which is our central object of study, is given by (1.1) and (1.2) as

$$E(x,y,z) = \frac{1}{2\pi}\int_{-\infty}^{\infty} \mathrm{d}\xi \int_{-\infty}^{\infty} \mathrm{d}\eta \exp\left[\mathrm{i}\{\xi^3 - 3\xi\eta^2 - z(\xi^2+\eta^2) - x\xi - y\eta\}\right]. \tag{1.7}$$

In § 2 we explain how this diffraction catastrophe can be realized optically in the space beyond a certain water droplet lens through which a parallel beam of light has been refracted. We display photographs of the intensity of the diffraction pattern in a series of sections corresponding to different values of z. These reveal a rich structure of diffraction maxima stacked in space like the atoms in the unit cells of a distorted crystal. The point maxima are separated by lines on which $|E|$ vanishes. These are the 'wavefront dislocations' introduced into wave theory by Nye & Berry (1974); they are the same as the 'quantized vortices' discussed by Riess (1970*a*, *b*, 1976), Hirschfelder & Christoph (1974), Hirschfelder, Goebel & Bruch (1974) and Hirschfelder & Tang (1976*a*, *b*).

It is the task of theory to explain the 'crystallography' of the diffraction pattern and the forms of the dislocation lines. The explanation begins in § 3 with a series of numerical computations of the integral (1.7), in the form of shaded contour maps of $|E|$ as a function of x and y for different values of z. They agree with the experimental photographs, even in the finest details. In § 4 a simple analytical theory of the function $E(x, y, z)$ is developed, valid inside the caustic, in terms of the sum of four interfering rays (in quantum mechanics this would correspond to the simplest semiclassical approximation); this four-wave theory is shown to explain the crystallography of the diffraction catastrophe. Finally, in § 5, the morphology of the dislocation lines, and in particular their change from hexagonally puckered rings near the z axis to 'hairpins' near the ribs, is explained quantitatively by the four-wave theory. The pattern of dislocation lines outside the caustic, which originate in interference involving complex rays, is also discussed.

2. Experiment

To realize the elliptic umbilic catastrophe by optical means, it was necessary to produce a wavefront corresponding to the potential function P given by (1.2). The fact that P, considered as a function of ξ and η, satisfies Poisson's equation, $\nabla^2 P = \text{constant}$, (so that its graph is a surface of constant curvature) suggested using a water droplet 'lens' to refract the light. In

Downloaded from rsta.royalsocietypublishing.org

addition, the fact that one of the contours of the cubic and quadratic part of P is an equilateral triangle suggested making the lens with a perimeter of this form; the elliptic umbilic is stable under perturbation, so that it was not necessary for the triangle to be precisely equilateral.

Therefore a hole whose shape approximated an equilateral triangle of side $L = 2.6$ mm was cut in adhesive tape stuck on to the horizontal surface of a glass microscope slide. A water droplet was allowed to fall on to the slide, where it formed a thin lens. This lens was illuminated from below (figure 1) with a parallel beam of laser light (wavelength $\lambda = 633$ nm) broadened so as to fill the aperture of the lens. After refraction the focused light formed an elliptic umbilic diffraction catastrophe a few centimetres above the lens.

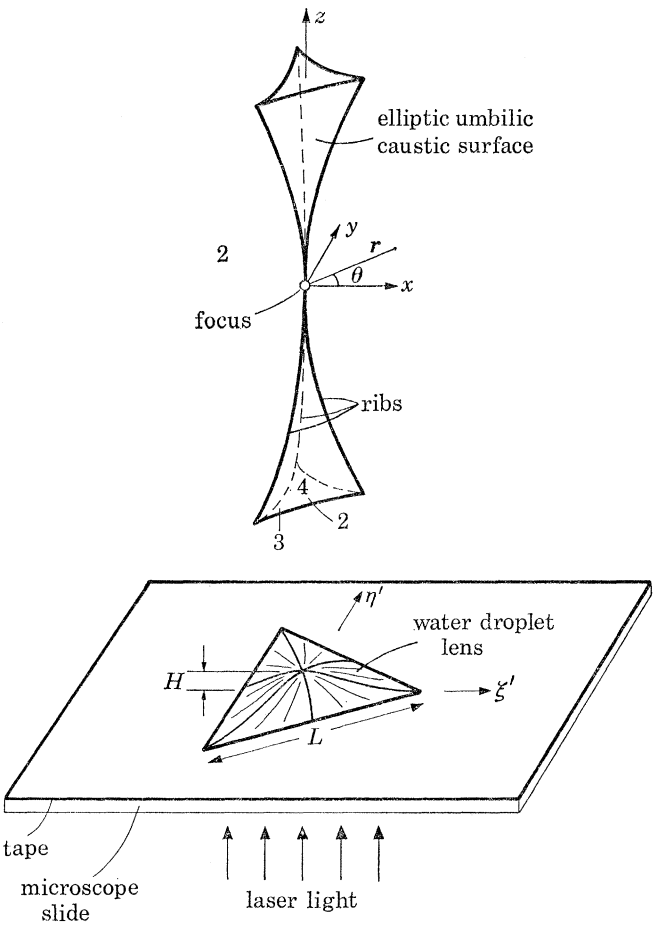

FIGURE 1. The elliptic umbilic caustic surface with dimensionless coordinates x, y, z, formed by the focusing of laser light refracted by a triangular water droplet lens in the $\xi'\eta'$ plane. Regions dominated by 2, 3 and 4 waves are indicated by the corresponding numbers. The splay of the caustic is exaggerated.

To see precisely why this should be so, consider the refracted wave as a complex scalar ψ; this could represent, say, the general electromagnetic field scalar of Green & Wolf (1953) and Wolf (1959, 1960), or simply one cartesian component of the electric or magnetic field. ψ is formed by the interference of wavelets from different parts of the lens. Let x', y', z' be Cartesian coordinates in space, with $z' = 0$ representing the upper surface of the microscope slide and $z' > 0$ the space above the lens. Let μ be the refractive index of water, and let the shape of the lens be defined by the function $h(\xi', \eta')$ giving its height above the point ξ', η' on the microscope slide. Then for an

Downloaded from rsta.royalsocietypublishing.org

incident plane wave of amplitude ψ_0 the Kirchhoff approximation of diffraction theory (Born & Wolf 1975) gives, for the refracted wave when $z' \gg h$,

$$\psi(x', y', z') = \frac{-i\psi_0}{\lambda} \int d\xi' \int d\eta' \frac{\exp\left[2\pi i\{\mu h(\xi', \eta') + \sqrt{([z' - h(\xi', \eta')]^2 + [x' - \xi']^2 + [y' - \eta']^2)}\}/\lambda\right]}{\sqrt{([z' - h(\xi', \eta')]^2 + [x' - \xi']^2 + [y' - \eta']^2)}}, \tag{2.1}$$

where the domain of integration is restricted to the illuminated triangular aperture in the ξ', η' plane. In writing (2.1) we have purposely omitted an irrelevant harmonic time factor. Because all refracted rays (or the directions of all plane-wave Fourier components of ψ) make small angles with the vertical it is permissible to expand the square roots with $z' - h$ as the dominant term. This gives the paraxial approximation to ψ:

$$\psi(x', y', z') = \frac{-i\psi_0}{\lambda z'} \exp\left[\frac{2\pi i}{\lambda}\left\{z' + \frac{x'^2 + y'^2}{2z'}\right\}\right] \times \int d\xi' \int d\eta' \exp\left[\frac{2\pi i}{\lambda}\left\{(\mu - 1)\, h(\xi', \eta') + \frac{\xi'^2 + \eta'^2}{2z'} - \frac{x'\xi'}{z'} - \frac{y'\eta'}{z'}\right\}\right]. \tag{2.2}$$

To find the lens shape $h(\xi', \eta')$ we realize that for the small width L and height H of the lens used in our experiment the form of the water surface is dominated by the surface tension γ and affected by gravity only to a negligible extent. Thus h satisfies Poisson's equation, namely

$$\partial^2 h/\partial\xi'^2 + \partial^2 h/\partial\eta'^2 = p/\gamma, \tag{2.3}$$

where p is the constant pressure inside the drop. The boundary conditions that h vanishes on the triangular perimeter of the aperture and $h = H$ at the centroid $\xi' = \eta' = 0$ of the aperture determine the value of p and lead to the following solution for h:

$$h(\xi', \eta') = H\{1 - 9(\xi'^2 + \eta'^2)/L^2 + 6\sqrt{3}(\xi'^3 - 3\xi'\eta'^2)/L^3\}. \tag{2.4}$$

The next step is to employ this form of $h(\xi', \eta')$ in (2.2) and change the variables of integration to

$$\xi \equiv (H'/\lambda)^{\frac{1}{3}} \xi'/L; \quad \eta \equiv (H'/\lambda)^{\frac{1}{3}} \eta'/L, \tag{2.5a}$$

with

$$H' \equiv 12\pi\sqrt{3} H(\mu - 1). \tag{2.5b}$$

Finally, the integration will be allowed to range over the whole ξ, η plane instead of being restricted to the (scaled) triangular aperture. Physically this implies the neglect of edge waves, a procedure justified in appendix A. The wave ψ now becomes

$$\psi(x', y', z') = \frac{-2\pi i\psi_0 L^2}{z'\lambda^{\frac{1}{3}} H'^{\frac{2}{3}}} \exp\left[2\pi i\{z' + H(\mu - 1) + (x'^2 + y'^2)/2z'\}/\lambda\right] E(x(x', z'), y(y', z'), z(z')), \tag{2.6}$$

where E is precisely the elliptic umbilic diffraction catastrophe defined by (1.7), involving the control parameters

$$x = \frac{2\pi L x'}{\lambda^{\frac{2}{3}} z' H'^{\frac{1}{3}}}, \quad y = \frac{2\pi L y'}{\lambda^{\frac{2}{3}} z' H'^{\frac{1}{3}}}, \quad z = \frac{\pi\sqrt{3}}{2z'}\left(\frac{H'}{\lambda}\right)^{\frac{1}{3}}\left(z' - \frac{L^2}{18H(\mu - 1)}\right). \tag{2.7}$$

Equation (2.6) shows that, apart from the factor $1/z'$, the amplitude of $\psi(x', y', z')$ is proportional to the amplitude of $E(x, y, z)$; thus it is the amplitude pattern of the diffraction integral E that we have to study. It must be remembered, however, that the phase of the actual wave

Downloaded from rsta.royalsocietypublishing.org

field ψ differs from that of E. (2.7) shows that the x, y, z coordinates in E are simply scaled cartesian coordinates centred on the focus, which occurs at the height

$$z' = L^2/18H(\mu - 1). \tag{2.8}$$

The occurrence of λ in the denominators of (2.7) means that as $\lambda \to 0$ all features of E (diffraction maxima, dislocation lines, etc.) flow towards the focus. However, this flow is faster in the x' and y' directions than in the z' direction, so that for very short wavelengths what should be observed in this experiment is the standard diffraction pattern greatly elongated, relatively speaking, in the z direction.

Sections through the diffraction catastrophe were photographed through a microscope imaging an $x'y'$ plane with a *fixed* value of z'. As the water droplet evaporated H got smaller, and the elliptic umbilic focus (2.8) was swept up through the imaged plane. Some of the resulting photographs are shown on figures 2*a–i* (plates 1–3) in a sequence moving away from the focus, i.e. unfolding the elliptic umbilic.

The focal section (figure 2*a*) shows a bright central patch, roughly triangular, surrounded by interference fringes receding to asymptotes making angles θ of $\pm\frac{1}{3}\pi$ and π with the positive x direction (vertical in the page). In the next photograph (2*b*) there is a brightening across the fringes in directions between the asymptotes, i.e. for $\theta = 0$ and $\pm\frac{2}{3}\pi$. This is the first indication of the cusps which are the sections of the ribs of the elliptic umbilic (figure 1), and which will come to dominate the patterns for fully unfolded sections (z large). It was a surprise that the asymptotes of the fringes in the focal section lay between, rather than along, the cusp directions.

In the next section (2*c*) the central maximum has turned into a bright hexagon and the nascent cusps have become more pronounced. In subsequent sections the cusps recede from the centre of the pattern, the area inside the caustic increases, and more hexagons, dark as well as bright, appear within the expanding caustic. In sections at large z these hexagons are arranged in a symmetrical array, and if a particular hexagon is observed while z is increased, it alternates between bright and dark. The implication of this is that the diffraction maxima and minima within the caustic are stacked in space like the atoms in a crystal lattice: in § 4 we shall study in detail the crystallography of this structure, and show how the lattice planes are, in fact, slightly curved.

The fringes parallel to the arcs of the caustic arise from the fold diffraction catastrophe first studied by Airy (1838), and the superposition of the three sets of such fringes inside the caustic is responsible for the array of hexagons. If it were not for the curvature of the lattice the number of hexagons in any plane would be a triangular number $\frac{1}{2}n(n+1)$, where n is the number along a side. Outside the caustic the original fringes that dominated the focal section can still be seen, but they are very close together and faint in comparison with the hexagons and the cusp diffraction maxima. In the final section (figure 2*i*) the cusps have come to dominate the pattern and are clothed with the characteristic diffraction structure studied by Pearcey (1946) (see also appendix C).

The dark hexagons have bright centres. This suggests that dislocation lines (where $|E|$ vanishes) within the caustic take the form of rings stacked in space. However, for very large z the diffraction near the ribs must be that described by Pearcey (1946), for which the dislocations (appendix C) are lines parallel to the ribs. Therefore the dislocations must change their topology as the ribs are approached: exactly how this happens will be explained in § 5.

Downloaded from rsta.royalsocietypublishing.org

3. Computations

The diffraction integral $E(x, y, z)$ or $E(r, \theta, z)$ (equation (1.7)) has useful symmetry properties, namely

$$E(x, y, -z) = E^*(x, y, z), \tag{3.1}$$

$$E(r, \theta + \tfrac{2}{3}n\pi, z) = E(r, \theta, z), \tag{3.2}$$

and

$$E(r, -\theta, z) = E(r, \theta, z), \tag{3.3}$$

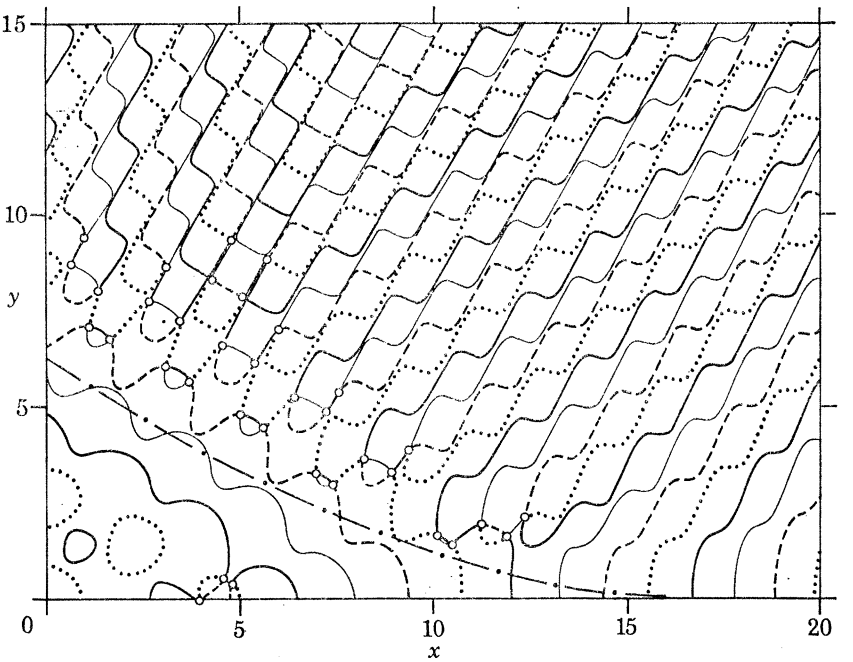

Figure 4. Equiphase lines of the diffraction function E at intervals of $\frac{1}{2}\pi$ in one quadrant of the xy plane for a typical value of $z = 4$. The caustic is shown by a chain line, and the dislocations are encircled.
—— 0; —— $\frac{1}{2}\pi$; – – – π; ..... $-\frac{1}{2}\pi$.

where r, θ are polar coordinates corresponding to x, y and n is an integer. The first is obvious by inspection of (1.7) and the second and third are easily derived by writing the integral in terms of polar coordinates in the ξ, η plane. Taken together, these relations imply that E has the same symmetry as the caustic (figure 1) apart from a change in the sign of the phase of E from z to $-z$ (which means that $E(x, y, 0)$ is real). Therefore it is necessary to compute E only for $z \geqslant 0$ and $0 \leqslant \theta \leqslant \frac{1}{3}\pi$.

By a method to be explained at the end of this section, E was first computed as a function of x and y for $z = 0, 1, 2, 3, 3.55, 3.85, 4, 5$ and 6. For comparison with the experimental photographs (figure 2), contours of the modulus $|E|$ were plotted at intervals of 0.05 and the resulting maps shaded in six different greys getting lighter as $|E|$ increased. These simulations are shown in figures 3*a–i* (plates 1–3). They may be compared with figure 2, because according to equations (2.6) and (2.7) the forms of $|\psi|$ and $|E|$ are virtually identical near the focus. It is clear that theory and experiment are in very close agreement.

Figure 4 shows the equiphase lines of E for a typical section with $z = 4$ for one quadrant of the xy plane. Dislocation lines in xyz intersect the xy planes at points that are clearly visible (and encircled) on the phase map as crossings of the different equiphase lines (cf. fig. 11 of Nye &

Downloaded from rsta.royalsocietypublishing.org

Berry 1974). The phase factor in equation (2.6) shows that the phase patterns of ψ and E are different, although the positions of their dislocations are the same. The chain line on figure 4 shows the caustic, where the light intensity according to geometrical optics would be infinite.

Of all these sections, the only one for which E can be expressed in terms of standard tabulated functions in closed form is the symmetry plane $z = 0$. Then an argument given in appendix B shows that

$$E(x, y, 0) = (\tfrac{2}{3})^{\frac{2}{3}}\pi \operatorname{Re}\left\{\operatorname{Ai}\left(\frac{-x-iy}{12^{\frac{1}{3}}}\right)\operatorname{Bi}\left(\frac{-x+iy}{12^{\frac{1}{3}}}\right)\right\}, \tag{3.4}$$

where Ai and Bi are the standard linearly independent Airy functions (Abramowitz & Stegun 1964, p. 446). This result was derived independently by Trinkaus & Drepper (1977).

There are, however, three more symmetry planes of E, namely that for which $y = 0$ and the two others obtained from it by rotation through $\frac{2}{3}\pi$ about the z axis. Although these planes cannot be studied by the optical experiment described in § 2 they furnish useful information about the crystallography and the dislocation structure of the diffraction catastrophe. Therefore on figures 5*a* (plate 4) and 5*b* respectively we plot the modulus (shaded as in figure 3) and phase of $E(x, 0, z)$ for $z \geqslant 0$. The chain lines represent the caustic; the left hand part has equation

$$x = -\tfrac{1}{3}z^2 \tag{3.5}$$

and is the intersection of $y = 0$ with one of the fold surfaces (figure 1), while the right hand part has equation

$$x = z^2 \tag{3.6}$$

and is one of the three ribs. The dislocations show up clearly on figure 5*b* as singularities of the phase (encircled), which correspond to zeros of $|E(x, 0, z)|$ lying within the black regions of figure 5*a*. Note that the x and z scales are considerably different on all xz plots.

In all these computations the method was as follows. First E (equation (1.7)) was reduced to a one-dimensional integral by exploiting the fact that η appears only to second degree in the exponent of the integrand. The complex Gaussian integral over η depends on the sign of $3\xi + z$; taking careful account of this sign and replacing ξ by the new variable

$$u \equiv \sqrt{\pm(\xi + \tfrac{1}{3}z)} \tag{3.7}$$

respectively for $\xi \gtrless -\frac{1}{3}z$, leads to

$$E(x, y, z) = \frac{\exp[i(\frac{1}{3}xz - 4z^3/27)]}{\sqrt{(3\pi)}}\left\{e^{-\frac{1}{4}i\pi}\int_0^\infty du \exp[i(u^6 - 2zu^4 + (z^2 - x)u^2 + y^2/12u^2)]\right.$$
$$\left. + e^{\frac{1}{4}i\pi}\int_0^\infty du \exp[-i(u^6 + 2zu^4 + (z^2 - x)u^2 + y^2/12u^2)]\right\}. \tag{3.8}$$

Each integral was evaluated separately. The divergence of the phase at $u = 0$ and $u = \infty$ was dealt with by splitting the domain of u into three regions: (i) $0 < u < u_1$; (ii) $u_1 \leqslant u \leqslant u_2$; (iii) $u_2 < u < \infty$. u_1 was chosen sufficiently small, and u_2 sufficiently large, that for the values of x, y, z being considered the regions (i) and (iii) contained no stationary points of the function in the exponent of the integrand. Then the integrals (i) and (iii) were evaluated asymptotically by integrating by parts (Dingle 1973), and the first three terms in the asymptotic expansion retained, u_1 and u_2 having been chosen to ensure this gave adequate accuracy. The integral (ii) was evaluated numerically by a method used by R. Saktreger (private communication). This consisted of dividing the range into sub-intervals small enough for the phase to be replaced by a linear function of u, and then evaluating the sub-integrals analytically. (The sub-intervals were optimized by the method of Richardson extrapolation.) The result of this procedure was a determination of E for all x, y, z with an estimated absolute error of less than 0.01.

Downloaded from rsta.royalsocietypublishing.org

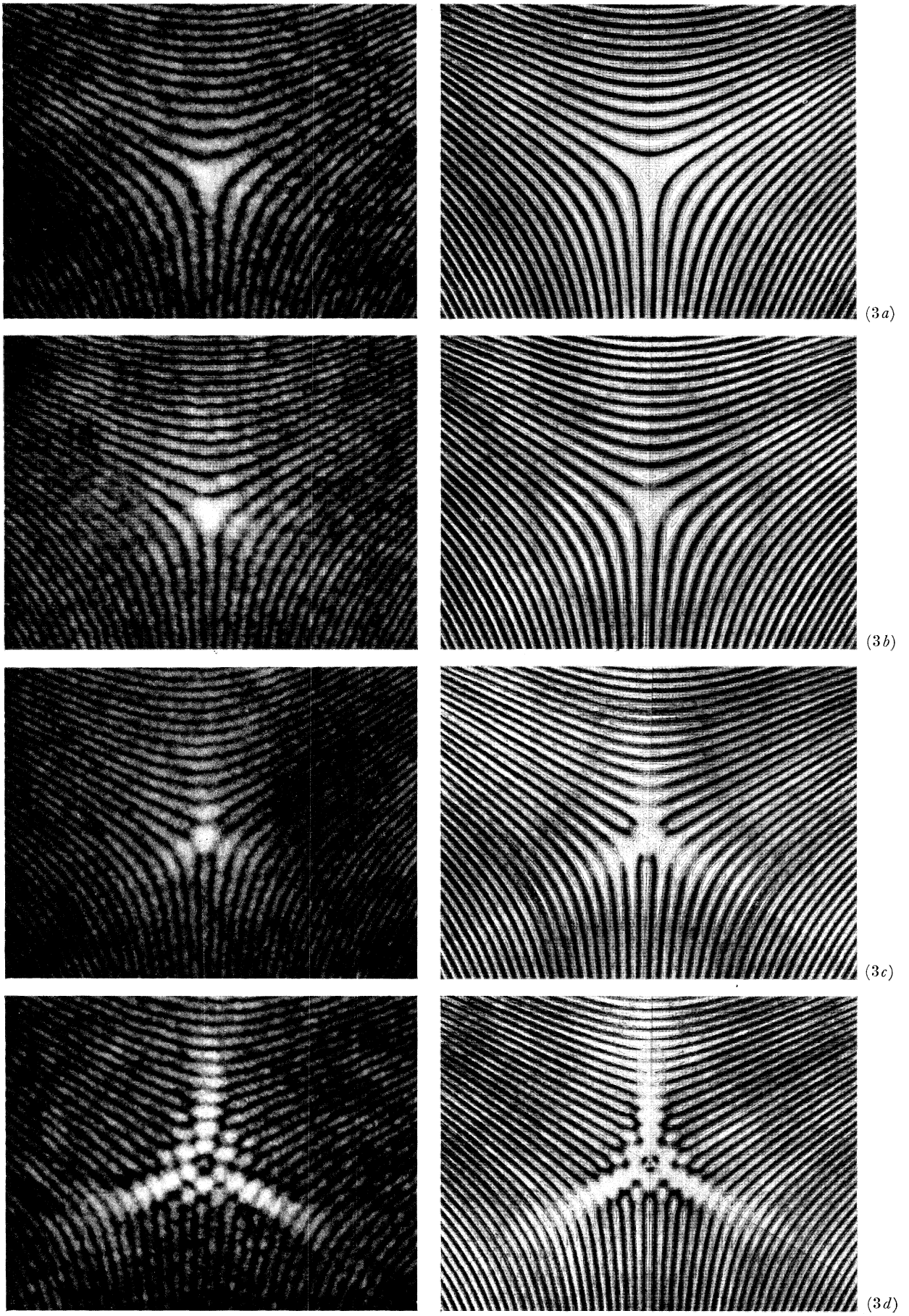

FIGURES 2*a–d* AND 3*a–d*. For description see plate 3.

(*Facing p.* 460)

PHILOSOPHICAL TRANSACTIONS OF THE ROYAL SOCIETY A MATHEMATICAL, PHYSICAL & ENGINEERING SCIENCES

PHILOSOPHICAL TRANSACTIONS OF THE ROYAL SOCIETY A MATHEMATICAL, PHYSICAL & ENGINEERING SCIENCES

Downloaded from rsta.royalsocietypublishing.org

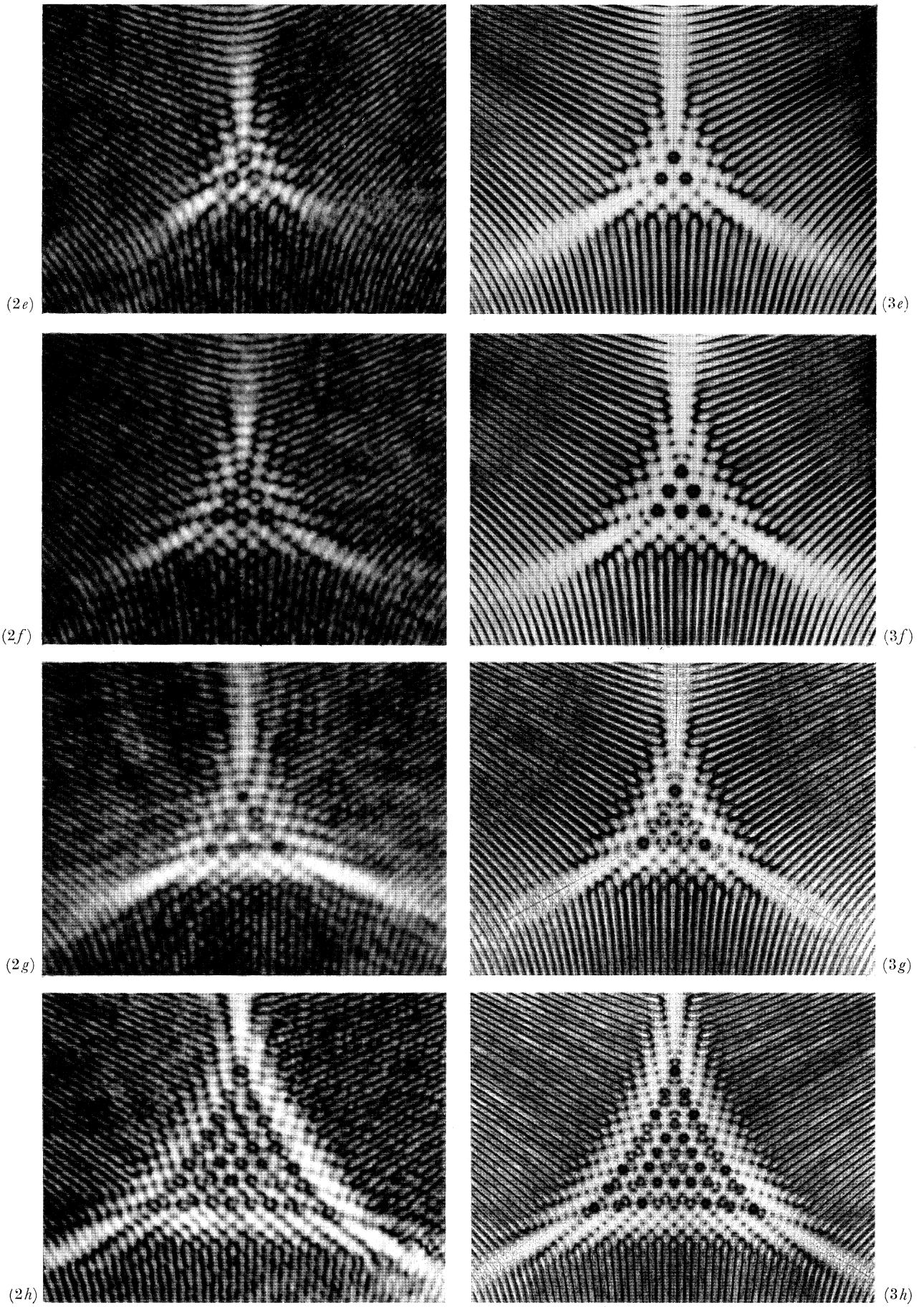

FIGURES 2*e–h* AND 3*e–h*. For description see plate 3, opposite.

PHILOSOPHICAL TRANSACTIONS OF THE ROYAL SOCIETY A MATHEMATICAL, PHYSICAL & ENGINEERING SCIENCES

PHILOSOPHICAL TRANSACTIONS OF THE ROYAL SOCIETY A MATHEMATICAL, PHYSICAL & ENGINEERING SCIENCES

Downloaded from rsta.royalsocietypublishing.org

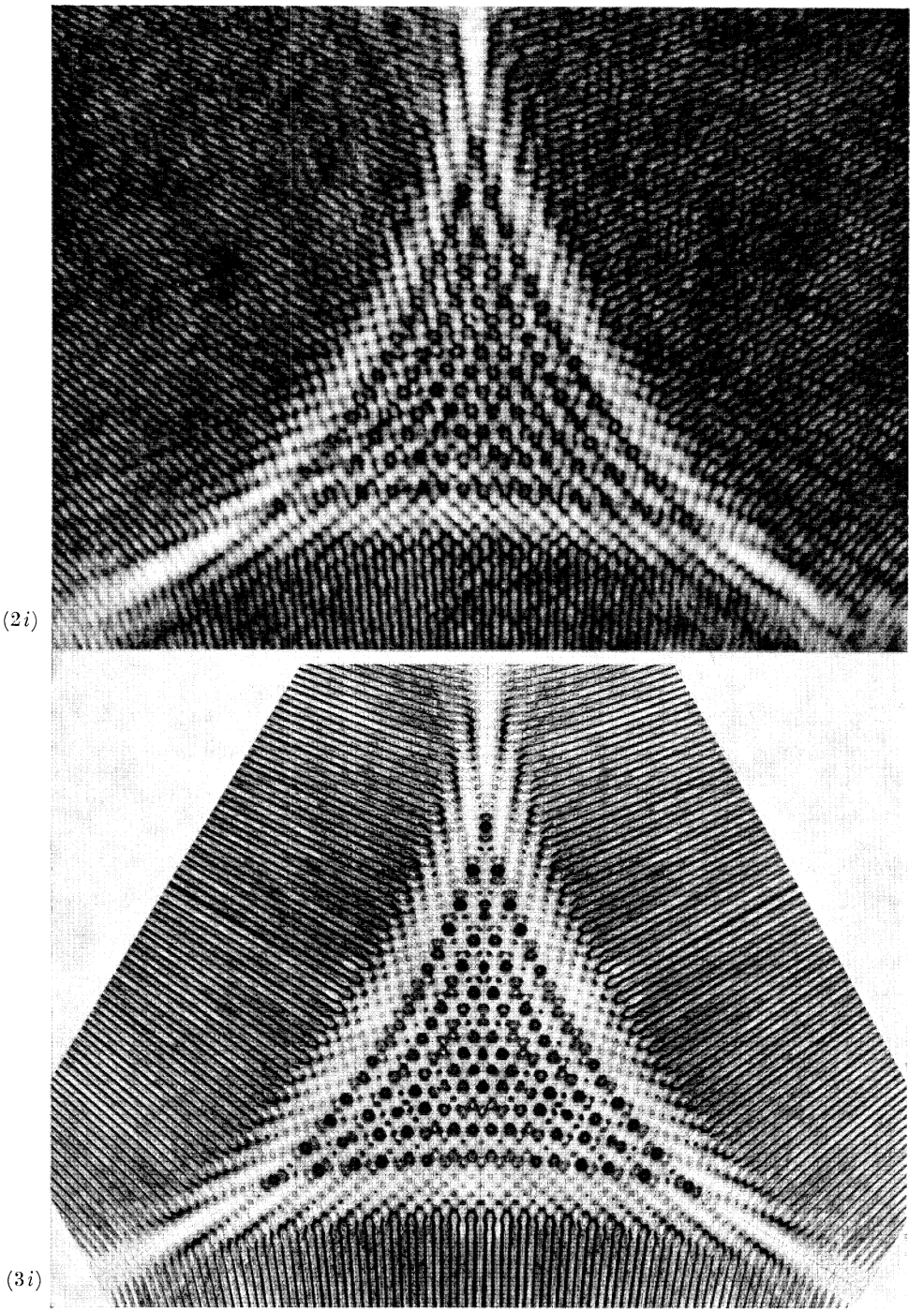

FIGURE 2. Photographs of sections (*a*–*i*) of the elliptic umbilic diffraction catastrophe. Section *a* is through the focus ($z = 0$) and sections *b*–*i* show the unfoldings as z increases. Sections *d*, *e*, *f* show successive triangular numbers (1, 3, 6) of dark hexagons. The x axis points vertically up the page. The length of the side of the caustic triangle in 2*i* is 0.17 mm. z values are (*a*), 0; (*b*), 1; (*c*), 2; (*d*), 3; (*e*), 3.55, (*f*), 3.85; (*g*), 4.0; (*h*), 4.90; (*i*), 5.81.

FIGURE 3. Computer simulations of sections (*a*–*i*) of the elliptic umbilic diffraction catastrophe for comparison with the observations in figure 2. Contour plots of the modulus $|E|$ of the diffraction integral (1.7) at 0.05 intervals were shaded as follows: $0 \leqslant$ black $< 0.05 <$ dark grey $< 0.1 <$ medium dark grey $< 0.15 <$ mid-grey $< 0.2 <$ light grey $< 0.25 <$ white. The x axis points vertically up the page. z values are (*a*), 0; (*b*), 1; (*c*), 2; (*d*), 3; (*e*), 3.55; (*f*), 3. 85; (*g*), 4; (*h*), 5; (*i*), 6.

PHILOSOPHICAL TRANSACTIONS OF THE ROYAL SOCIETY A MATHEMATICAL, PHYSICAL & ENGINEERING SCIENCES

PHILOSOPHICAL TRANSACTIONS OF THE ROYAL SOCIETY A MATHEMATICAL, PHYSICAL & ENGINEERING SCIENCES

Downloaded from rsta.royalsocietypublishing.org

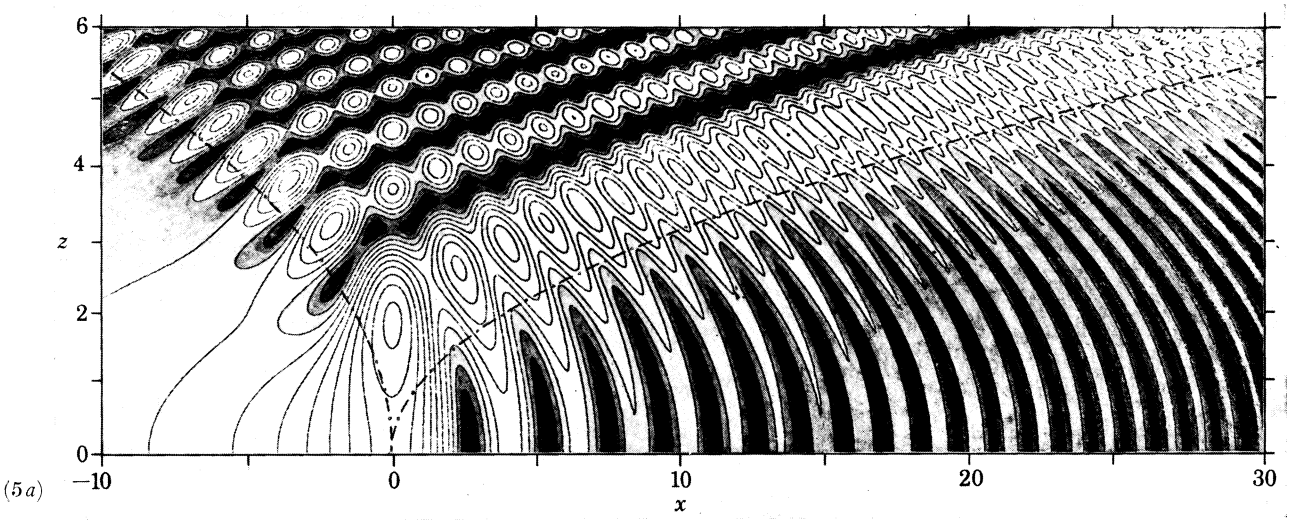

FIGURE 5*a*. For description see opposite.

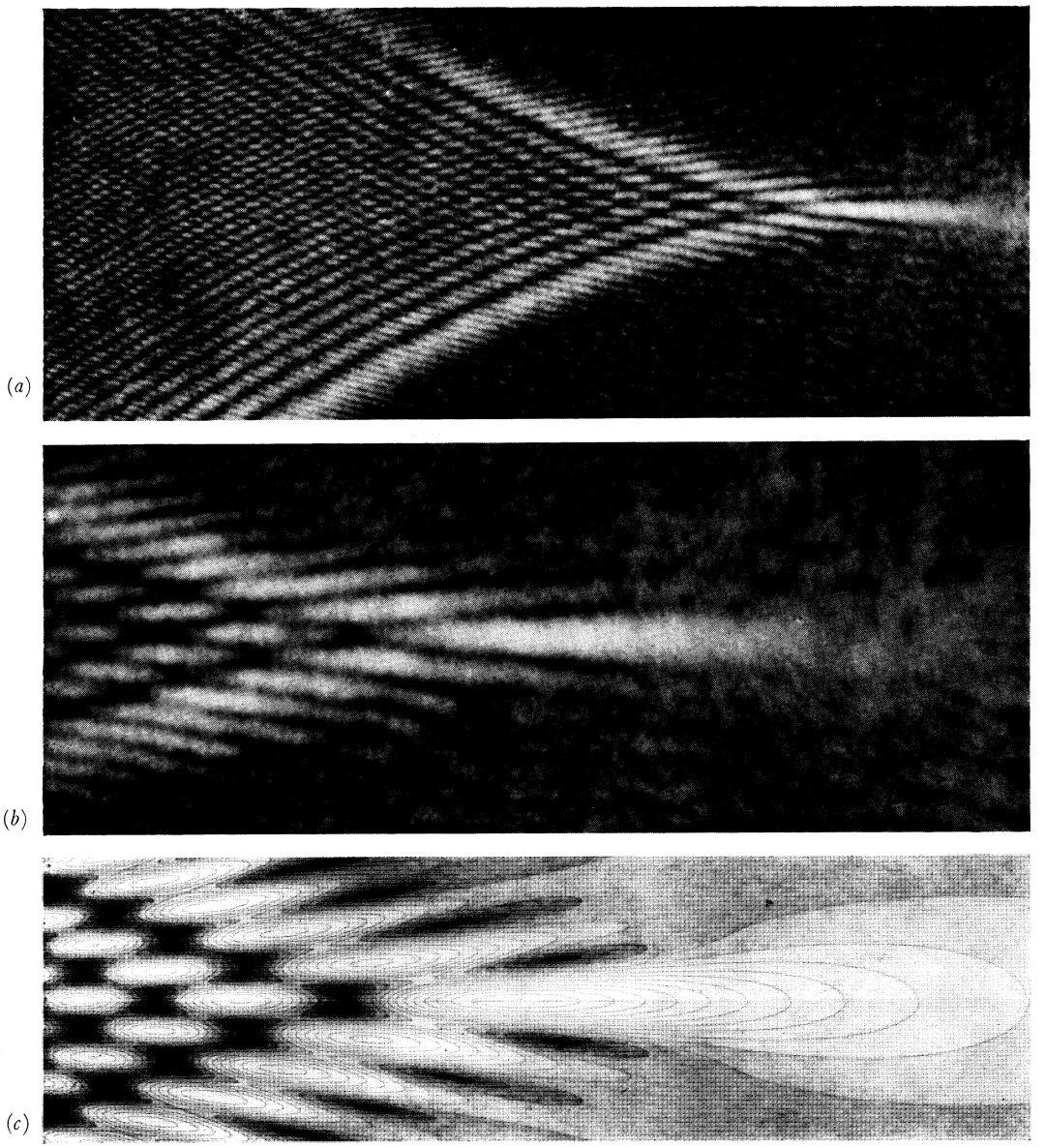

FIGURE 13. For description see opposite.

PHILOSOPHICAL TRANSACTIONS OF THE ROYAL SOCIETY A MATHEMATICAL, PHYSICAL & ENGINEERING SCIENCES

PHILOSOPHICAL TRANSACTIONS OF THE ROYAL SOCIETY A MATHEMATICAL, PHYSICAL & ENGINEERING SCIENCES

Downloaded from rsta.royalsocietypublishing.org

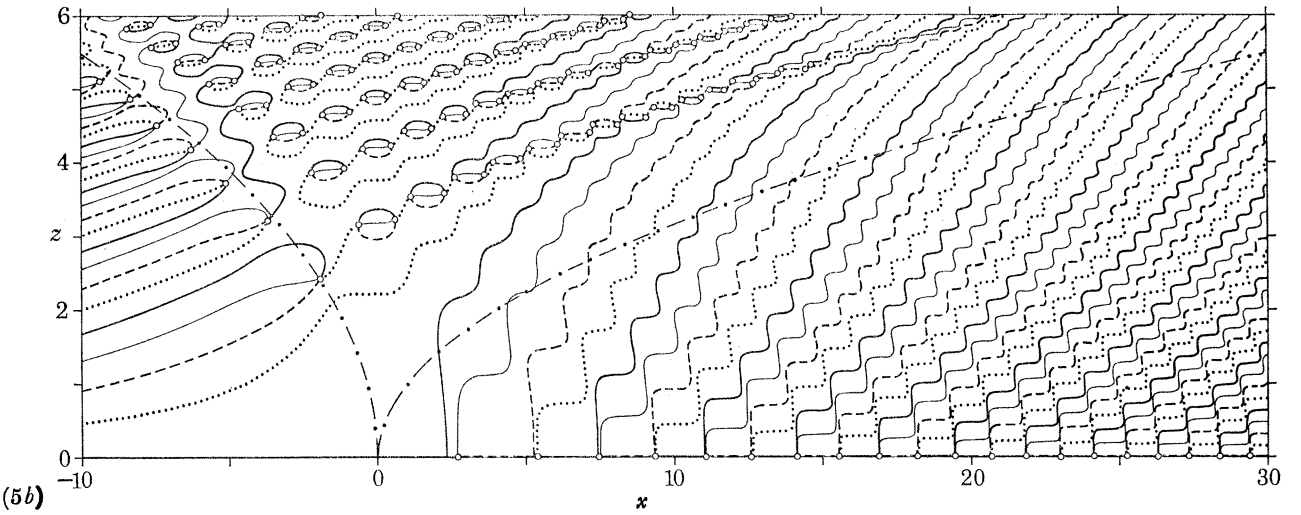

FIGURE 5. (*a*) Contours of modulus $|E(x, 0, z)|$ at 0.05 intervals, shaded as in figure 3. (*b*) Equiphase lines of $E(x, 0, z)$ at $\frac{1}{2}\pi$ intervals, represented as in figure 4; the dislocations are encircled. The caustic is shown by a chain line. Note that the x and z scales are considerably different.

4. FOUR-WAVE THEORY: 'CRYSTALLOGRAPHY' OF THE DIFFRACTION PATTERN

Each point within the elliptic umbilic caustic surface is illuminated by four rays. In the experiment described in § 2 these come from different parts of the droplet. Mathematically the rays correspond to distinct solutions of the gradient mapping equations (1.3). To a close approximation the interference-pattern that results from adding the waves associated with the rays is given by evaluating $E(x, y, z)$ (equation 1.7) by the method of two-dimensional stationary phase (Born & Wolf 1975, appendix III; Dingle 1973, chapter IX).

Because of the symmetry (equation (3.1)), we only need consider $z \geqslant 0$. It is simplest to consider first points for which x and y are small and z is large: a case for which the approximate stationary-phase expression for E can be written down explicitly. This will show how the features of the diffraction pattern are arranged on a lattice in space. After the symmetry of this pattern has been established it will be possible to explain the observations far from the z axis (e.g. near the caustic) in terms of distortions of the basic lattice.

On the z axis itself (i.e. for $x = y = 0$) the four solutions of (1.3) are easily found to be

$$\xi_1 = -\tfrac{1}{3}z, \quad \eta_1 = \tfrac{1}{\sqrt{3}}z; \quad \xi_2 = -\tfrac{1}{3}z, \quad \eta_2 = -\tfrac{1}{\sqrt{3}}z; \quad \xi_3 = \tfrac{2}{3}z, \quad \eta_3 = 0; \quad \xi_4 = \eta_4 = 0. \tag{4.1}$$

The first three rays come from the vertices of an equilateral triangle in the ξ, η plane, centred on the origin $\xi = \eta = 0$, while the fourth ray comes from the origin itself. The method of stationary phase involves the Hessian determinant of $P(\xi, \eta; x, y, z)$ (this is simply the left hand side of

DESCRIPTION OF FIGURE 13

FIGURE 13. (*a*) Micrograph of the cusp diffraction catastrophe. Width of field of view 0.45 mm. (*b*) Detail of (*a*); the vertical separation of the close dislocation pairs is 3 μm. (*c*) Theoretical cusp diffraction catastrophe: computer simulation of (*b*).

Downloaded from rsta.royalsocietypublishing.org

equation (1.4)) evaluated at the stationary points; careful consideration must be paid to the sign of this quantity. Standard analysis using the method of stationary phase then yields

$$E(0,0,z) \approx -\tfrac{1}{2}\mathrm{i}\{\sqrt{3}\exp[\mathrm{i}(\tfrac{1}{2}\pi - 4z^3/27)] + 1\}/z. \tag{4.2}$$

The first term combines the equal contributions from rays 1, 2 and 3, each of which has strength proportional to $\frac{1}{\sqrt{3}}$, while the second term arises from ray 4 whose strength is proportional to unity.

This expression shows that E never vanishes on the z axis, but reaches minima with amplitude

$$|E_{\min}| \approx \tfrac{1}{2}\{\sqrt{3}-1\}/z \tag{4.3}$$

at heights

$$z_n \approx 3\{\tfrac{1}{4}(2n-\tfrac{1}{2})\,\pi\}^{\frac{1}{3}} = 3.4873(n-\tfrac{1}{4})^{\frac{1}{3}}, \quad n = 1, 2, 3, \ldots, \tag{4.4}$$

which agree very well with the positions of minima on figure 5*a*. The minima will turn out to be the centres of dark hexagons. Between the minima are maxima with amplitude

$$|E_{\max}| \approx \tfrac{1}{2}\{\sqrt{3}+1\}/z. \tag{4.5}$$

Taking one of the minima z_n as origin and writing

$$z \equiv z_n + Z, \tag{4.6}$$

it is clear that $E(0,0,Z)$ is approximately periodic in Z with local repeat distance

$$\Delta z = \tfrac{9}{2}\pi z_n^{-2}. \tag{4.7}$$

The periodicity is more nearly exact for larger n. In real space the vertical repeat distance $\Delta z'$ can be obtained from the scaling law (2.7) which gives

$$\Delta z' = 0.0051 L^2 \lambda^{\frac{1}{3}} \Delta z / \{H(\mu-1)\}^{\frac{4}{3}}. \tag{4.8}$$

When x and y are not zero but still sufficiently small in comparison with z the mapping (1.3) can be solved to first order in x, y by applying perturbation theory to the four rays given by (4.1). After some algebra the resulting stationary-phase expression for E is

$$E(x,y,Z) \approx \frac{-\mathrm{i}}{2z_n}\left\{1 - \tfrac{1}{\sqrt{3}}\exp[-2\pi\mathrm{i}(Z/\Delta z + 2x/\Delta x)]\left(2\exp[6\pi\mathrm{i}x/\Delta x]\cos\frac{2\sqrt{3}\,\pi y}{\Delta x} + 1\right)\right\}, \tag{4.9}$$

where Δx, defined by

$$\Delta x \equiv 6\pi/z_n, \tag{4.10}$$

is the x repeat distance of the pattern. The result (4.9) could have been obtained in an alternative way by adding three plane waves whose wave vectors are symmetrically disposed about the z axis, and which have strength $\frac{1}{\sqrt{3}}$, to a fourth plane wave travelling along the z axis and of strength 1.

In real space the x' repeat distance $\Delta x'$ can be obtained from (2.7) as

$$\Delta x' = 0.036 L \lambda^{\frac{2}{3}} \Delta x / \{H(\mu-1)\}^{\frac{2}{3}}. \tag{4.11}$$

Taken together with (4.8) this defines an elongation ratio

$$R \equiv \frac{\Delta z'/\Delta z}{\Delta x'/\Delta x} = \frac{0.142L}{\lambda^{\frac{1}{3}}\{H(\mu-1)\}^{\frac{2}{3}}} \tag{4.12}$$

relating the shapes of figures in xz and $x'z'$. In a typical case ($L \approx 5\,\mathrm{mm}$, $\lambda \approx 6\times10^{-4}\,\mathrm{mm}$, $H \approx 0.1\,\mathrm{mm}$) $R \approx 50$, so that the elongation along z' is in fact quite large. Physically the large values of R arise because the three waves, travelling in directions close to the z axis, form a pattern with repeat along z of slightly more than λ, which beats with the single wave, whose repeat

Downloaded from rsta.royalsocietypublishing.org

distance is λ, to give a z repeat distance in the final pattern large in comparison with the x repeat distance.

The crystallography of the diffraction pattern observed near the z axis, as defined by the space group of the modulus $|E|$, can be established from three basic properties of $E(x, y, Z)$ derivable from (4.9):

Property R. E has a primitive rhombohedral unit cell (figure 6) whose diagonal is directed along the z direction. This follows from these symmetries of equation (4.9):

$$\left.\begin{aligned} E(x,y,Z) &= E(x+\tfrac{1}{3}\Delta x,\ y,\ Z+\tfrac{1}{3}\Delta z) \\ &= E(x-\tfrac{1}{6}\Delta x,\ y+\tfrac{1}{2\sqrt{3}}\Delta x,\ Z+\tfrac{1}{3}\Delta z) \\ &= E(x-\tfrac{1}{6}\Delta x,\ y-\tfrac{1}{2\sqrt{3}}\Delta x,\ Z+\tfrac{1}{3}\Delta z) \end{aligned}\right\}, \tag{4.13}$$

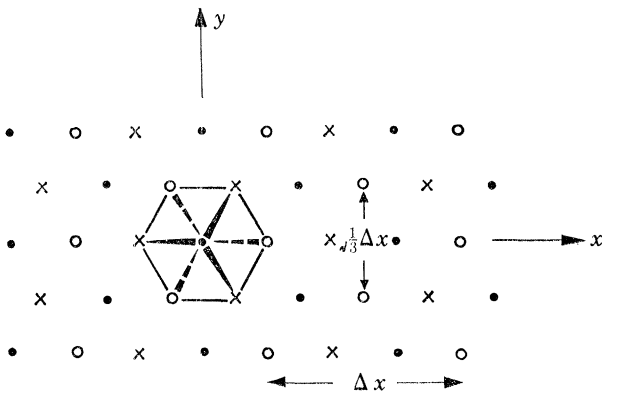

FIGURE 6. Lattice points (centres of dark hexagons) in x, y, Z space. The lines join the vertices of a rhombohedral unit cell, whose body diagonal lies along the Z direction and has length Δz. ●, $Z = 0$; ○, $Z = \frac{1}{3}\Delta z$; ×, $Z = \frac{2}{3}\Delta z$.

which define the three lattice vectors shown on figure 6 by broken arrows. We take the lattice points as images under these translations of the point $x = y = Z = 0$.

Property m. E has a mirror plane. In fact it has several, but it is sufficient to exhibit one of them. We choose $y = 0$, whose mirror property follows from

$$E(x, y, Z) = E(x, -y, Z). \tag{4.14}$$

Property $\bar{3}$. $|E|$ has an inverse threefold axis, i.e. $|E|$ is invariant under rotation through 120° about some axis followed by inversion through a point on the axis. To establish this we first note that the Z axis is an ordinary threefold axis for E; this follows from

$$E(x, y, Z) = E(-\tfrac{1}{2}x - \tfrac{\sqrt{3}}{2}y,\ -\tfrac{1}{2}y + \tfrac{\sqrt{3}}{2}x,\ Z). \tag{4.15}$$

Then we observe that inversion through the origin yields

$$E(x, y, Z) = -E^*(-x, -y, -Z). \tag{4.16}$$

Therefore although the phase of E does not have a $\bar{3}$ axis the modulus $|E|$ does.

It follows that the point group of $|E|$ is $\bar{3}$m. There are two space groups corresponding to this point group and a rhombohedral lattice, but only one of them has true reflexion planes (rather than glide reflexion planes) parallel to the Z axis; we can conclude that the space group is R$\bar{3}$m. The properties R, m and $\bar{3}$ imply many other symmetries of $|E|$ (e.g. screw triad axes, screw diad axes and glide planes), which are enumerated in International tables (1965, pp. 272, 273).

Downloaded from rsta.royalsocietypublishing.org

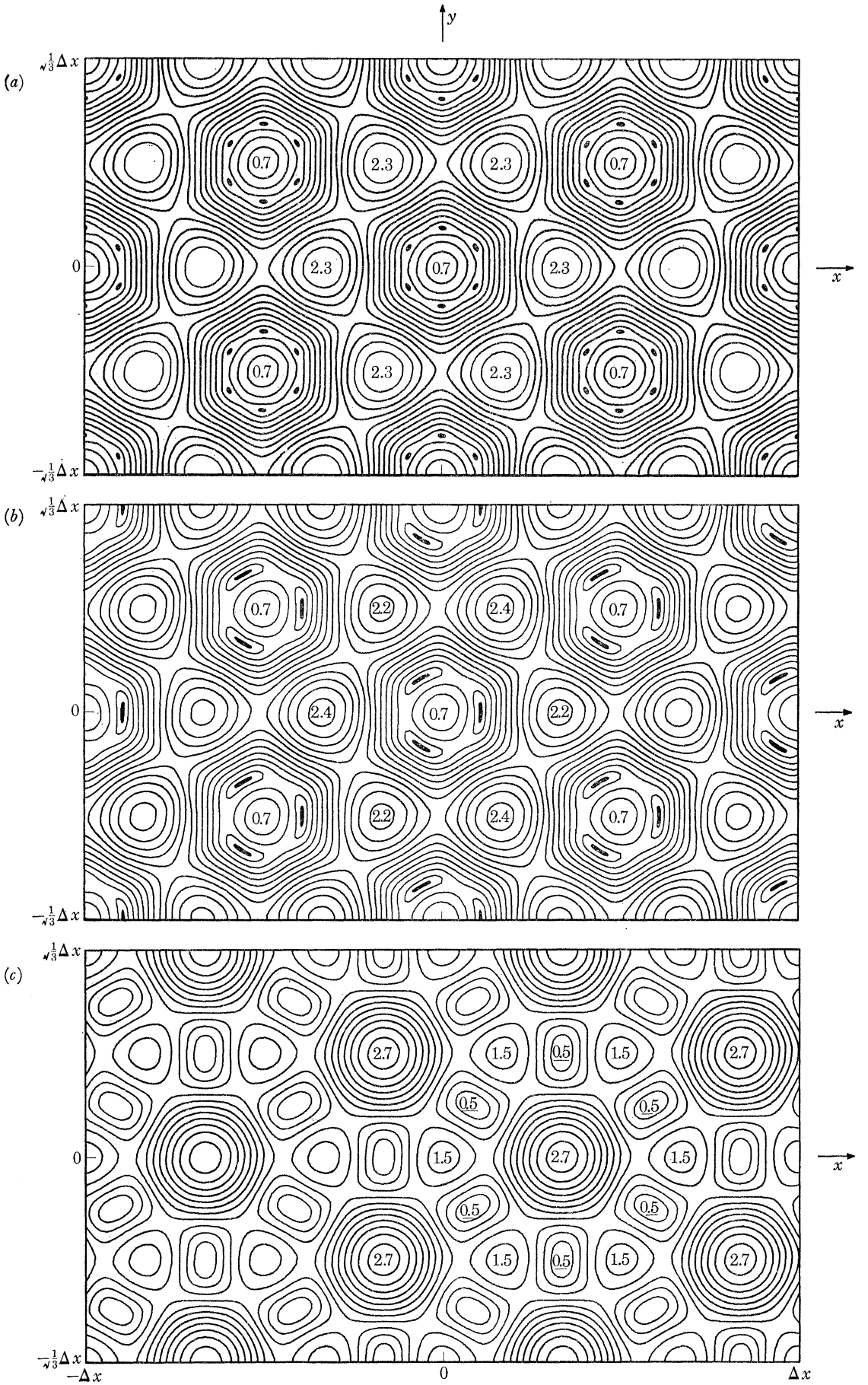

FIGURE 7. For description see opposite.

PHILOSOPHICAL TRANSACTIONS OF THE ROYAL SOCIETY A MATHEMATICAL, PHYSICAL & ENGINEERING SCIENCES

PHILOSOPHICAL TRANSACTIONS OF THE ROYAL SOCIETY A MATHEMATICAL, PHYSICAL & ENGINEERING SCIENCES

Downloaded from rsta.royalsocietypublishing.org

The appearance of complex conjugates in the relations (3.1) and (4.16) shows that the phase of E cannot have the same symmetry as the modulus $|E|$. In fact, the phase pattern possesses black-white symmetry (Birss 1964; Schubnikov & Koptsik 1974); this arises because phase can be positive or negative. However, we shall not discuss the details of the pattern of the phase of E, because the physical wave ψ is complicated by the presence of an extra phase factor (equation (2.6)) which destroys the symmetry.

What is observed in the experiment described in § 2 are sections of $|E(x, y, z)|$ for fixed z. So far as diffraction near the z axis is concerned the symmetries just discussed imply that all the different diffraction patterns in xy planes are contained between $Z = 0$ and $Z = \frac{1}{6}\Delta z$. The patterns for any other Z can be obtained from one of these by inversion through a centre of symmetry on the Z axis and/or translation along x. Inspection of contour maps of $|E(x, y, Z)|$ for fixed Z (figure 7), computed from (4.9), together with application of these symmetries, explains the alternation of bright and dark hexagons as Z varies with x and y held fixed.

Consider figure 7*a*, which shows the plane $Z = 0$. The origin $x = y = 0$ is the bright centre of a dark hexagon; the strength at the centre, as conveniently represented by the value of $2z|E|$, is 0.7. The hexagon's 'corners' point towards nearest-neighbour similar hexagons centred on lattice points. Surrounding each of these dark hexagons are six bright shapes whose central strength is 2.3; on figure 7*a* these shapes have contours looking like rounded triangles but the dark bars separating them might make them appear hexagonal to the eye. This arrangement of dark and bright hexagons can be seen on figure 2*i*; along the x axis (i.e. along any of the lines joining the centre to a cusp) the sequence of hexagons begins D B B D B B (D = dark, B = bright).

Figure 7*c* shows the plane $Z = \frac{1}{6}\Delta z$. Now the pattern is dominated by bright hexagons whose central strength is 2.7. Surrounding each of these are six dark rectangles (minima, central strength 0.5) alternating with six 'triangles' (maxima) with medium strength 1.5. Something of this structure is apparent near the three bright hexagons surrounding the centre of figure 3*g* (i.e. the computer simulation for $z = 4$).

Figure 7*b* shows the plane $Z = \frac{1}{36}\Delta z$, which was selected for a reason to be explained in the next section. This plane shows the generic feature of being only trigonally and not hexagonally symmetric about each dark 'hexagon' (central strength 0.7), in that the six surrounding bright 'hexagons' (i.e. barred triangles) alternate in central strength between 2.2 and 2.4.

The 'crystal lattice' we have been considering gets distorted on receding from the z axis towards the caustic. Without studying this distortion it is impossible to understand the observed diffraction near the caustic. Our method will be to extend the four wave theory of this section by removing the restriction that x must be small. However, an analytical solution is only possible when $y = 0$ and so we concentrate on this case, that is, we work out the exact four wave theory in the xz plane (and the two others related to it by symmetry). The basic mapping equations (1.3) have the solutions

$$\left.\begin{aligned} &\xi_1 = -\tfrac{1}{3}z,\ \eta_1 = \sqrt{\{\tfrac{1}{3}(z^2 - x)\}}; \quad \xi_2 = -\tfrac{1}{3}z,\ \eta_2 = -\sqrt{\{\tfrac{1}{3}(z^2 - x)\}};\\ &\xi_3 = \tfrac{1}{3}\{z + \sqrt{(z^2 + 3x)}\},\ \eta_3 = 0; \quad \xi_4 = \tfrac{1}{3}\{z - \sqrt{(z^2 + 3x)}\},\ \eta_4 = 0;\end{aligned}\right\} \tag{4.17}$$

FIGURE 7. Contours of $2z|E(x, y, Z)|$ at 0.2 intervals in the 'crystallographic' region (z large; x/z and y/z small) as computed from equation (4.9), for (*a*) $Z = 0$; (*b*) $Z = \frac{1}{36}\Delta z$; (*c*) $Z = \frac{1}{6}\Delta z$. Regions of strength less than 0.05 (which all contain a dislocation) are shown black. Local maxima are shown by their approximate values, and local minima (on 7 (*c*) only) are shown by their approximate values underlined.

Downloaded from rsta.royalsocietypublishing.org

these generalize the solutions in equation (4.1). On the fold ($x = -\frac{1}{3}z^2$) the roots 3 and 4 coalesce, while on the cusp ($x = z^2$) the roots 1, 2 and 4 coalesce. The method of stationary phase applied to equation (1.7) gives, after some algebra, the generalization of (4.2), namely

$$E(x,0,z) \approx \frac{\mathrm{i}\exp[\mathrm{i}(2W^3-9xz-2z^3)/27]}{2\sqrt{\{W(2z-W)\}}}\left\{2\sqrt{\left(\frac{W(2z-W)}{3(z^2-x)}\right)}\exp[-\mathrm{i}(\phi_1+\tfrac{1}{2}\pi)]\right.$$
$$\left.+\sqrt{\left(\frac{2z-W}{2z+W}\right)}\exp[-\mathrm{i}(\phi_2+\tfrac{1}{2}\pi)]-1\right\}, \quad (4.18)$$

where
$$\left.\begin{aligned} W &\equiv \sqrt{(z^2+3x)},\\ \phi_1 &\equiv \tfrac{2}{27}(W^3-9xz+z^3),\\ \phi_2 &\equiv \tfrac{4}{27}W^3. \end{aligned}\right\} \quad (4.19)$$

Now there are points (x, z) where $E(x, 0, z)$ vanishes; these are the intersections of dislocation lines with the plane $y = 0$ and will be discussed in detail in § 5. However, we are now interested in the lattice points of the distorted crystal, and these are determined by choosing the phases ϕ_1 and ϕ_2 to be integral multiples of 2π, apart from constants selected to ensure compatibility with the lattice points (4.4) on the z axis, as follows:

$$\phi_1(x,z) = (2m-\tfrac{1}{2})\,\pi, \quad \phi_2(x,z) = (2n-\tfrac{1}{2})\,\pi, \quad (4.20)$$

m and n being integers. For $x = 0$, $\phi_1 = \phi_2$ so that the lattice points on the z axis have $m = n$; these have already been discussed (equation (4.4)). When x is small, linear expansion of ϕ_1 and ϕ_2 in x gives precisely the lattice points of the 'perfect crystal' wave (4.9) (with $y = 0$). In this perfect crystal there are lattice planes with constant z. The lth such plane has points (in the plane $y = 0$) labelled by q, where in (4.20)

$$m = l-q, \quad n = l+2q; \quad (4.21)$$

this follows by inspection of the linearized version of (4.20). When x is not small these lattice points will lie on a surface that deviates from a plane. The form of the surface can be found by eliminating q, which gives

$$\phi_2(x,z)+2\phi_1(x,z) = 3\pi(2l-\tfrac{1}{2}). \quad (4.22)$$

By (4.19) this result implies that the horizontal lattice plane through $y = 0$, $z = z_0$ is distorted for large x into a surface with equation

$$\tfrac{8}{3}(z^2+3x)^{\frac{3}{2}}-12xz+\tfrac{4}{3}z^3 = 4z_0^3. \quad (4.23)$$

This has the following limiting forms:

$$z(x) = \begin{cases} (\frac{3}{4})^{\frac{1}{3}}z_0 = 0.909z_0 & (x = -\frac{1}{3}z^2, \quad \text{i.e. at the fold}),\\ z_0-\frac{3}{4}x^2/z_0^3 & (x \text{ small}),\\ (\frac{3}{8})^{\frac{1}{3}}z_0 = 0.721z_0 & (x = z^2, \qquad \text{i.e. at the cusp}). \end{cases} \quad (4.24)$$

Therefore the crystal is deformed so that its horizontal lattice 'planes' are convex away from the focus at $x = y = z = 0$. The deformation is very accurately parabolic, in that use of the second expression on the right hand side of (4.24) out to the fold and cusp gives $z(x)$ with an error of less than 4 %. The curved lattice planes are marked as broken lines on figure 8, on which bright regions are represented by the contour $|E| = 0.2$, and dark regions are represented schematically by the thick black S-shaped lines, the full significance of which will be explained in the next section.

Downloaded from rsta.royalsocietypublishing.org

To see how this distorted lattice explains the observed sequence of bright and dark hexagons, consider figure 2*i*. Along one of the symmetry lines the sequence from fold to cusp (i.e. from $x = -\frac{1}{3}z^2$ to $x = z^2$) is

$$\begin{pmatrix} \text{B} \\ \text{fold} \end{pmatrix} \text{DBDBDBBD} \underset{\text{(centre } x=0)}{\uparrow} \text{BBDBBBDBBBBDIBBBBBIDIBB} \ldots \begin{pmatrix} \text{B} \\ \text{cusp} \end{pmatrix}$$

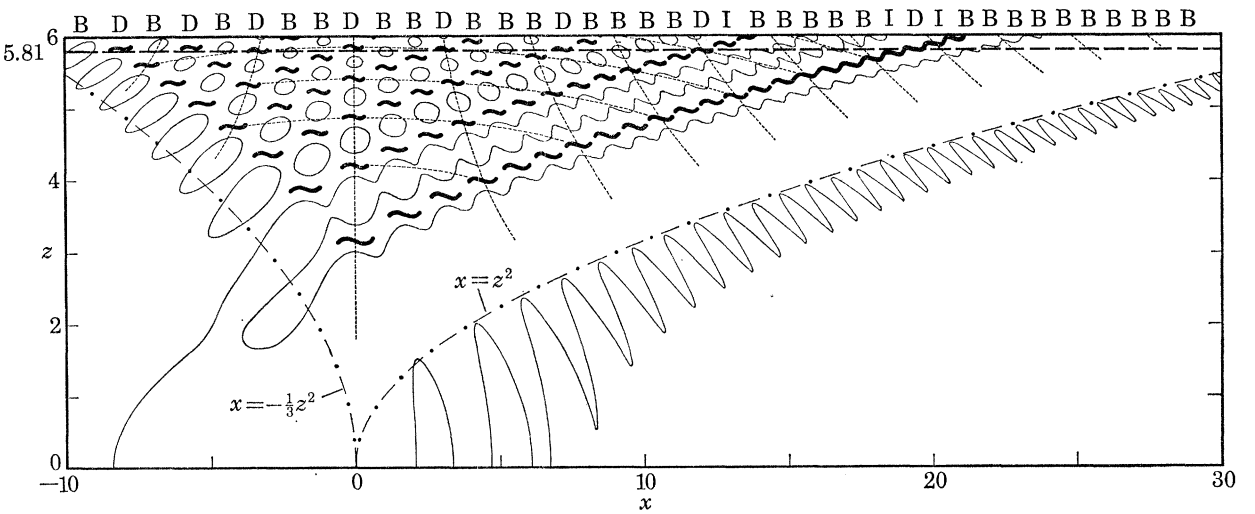

FIGURE 8. The *xz* plane as in figure 5 showing the caustic (chain line), the distorted lattice planes (broken lines), the contour $|E| = 0.2$ (thin line) and the projection of all dislocation lines inside the caustic which intersect the plane (thick lines), The line at $z = 5.81$ indicates the height of figure 2*i*, and each segment of the line represents a hexagon on figure 2*i*, whose brightness is indicated by B (bright), D (dark) or I (intermediate).

where B = bright, D = dark, I = intermediate. The dark centre means that the observation is near a plane where $x = y = 0$ is a lattice point. Therefore it is near one of the z values given by (4.4). In fact it is near $z_5 = 5.862$. The hexagon sequence can be read off from figure 8 along the broken horizontal line drawn at $z = 5.81$ just below z_5 for the best fit with the data; each section of the line represents a hexagon whose brightness is indicated along the top of the figure. Evidently the sequence given by this theoretical construction agrees closely with that observed.

Near the cusp the distorted lattice is so rotated that the x axis becomes almost parallel with a direction ($\langle 100 \rangle$ on rhombohedral axes) along which the dark hexagons are close packed. Thus the hexagons can be all bright or all dark. It is the resulting long sequences of bright and dark hexagons that merge together to give the bright and dark regions of the Pearcey cusp diffraction pattern (see appendix C).

5. WAVEFRONT DISLOCATIONS: RINGS AND HAIRPINS

Now we discuss the form of the 'dislocation lines', on which $|E|$ is zero and the phase of E is indeterminate. To do this we shall use the four-wave theory developed in § 4. Ultimately the validity of this procedure – which amounts to using a very simple approximation for E to locate the most delicate features of the diffraction catastrophe – can be justified only by comparison with exact computation of the fundamental integral (1.7). However, we base our confidence in the four-wave theory on the great accuracy, demonstrated in appendix C, of the corresponding three-wave theory in giving the dislocation points associated with the cusp. The significance of

Downloaded from rsta.royalsocietypublishing.org

the thick black lines on figure 8 is that they are the projections on to the plane $y = 0$ of all those dislocation lines which intersect that plane inside the caustic. Some were computed, by a variety of methods to be described, and the rest were sketched in by hand.

Consider first dislocations near the z axis far from the focus. Their form is given by the zeros of equation (4.9) and so must have (at least) the symmetry of the pattern that equation describes. The dislocations are thus the lines in x, y, Z satisfying

$$\exp[-2\pi i(Z/\Delta z + 2x/\Delta x)]\,(2\exp[6\pi i x/\Delta x]\cos(2\sqrt{3}\,\pi y/\Delta x) + 1) = \sqrt{3}. \tag{5.1}$$

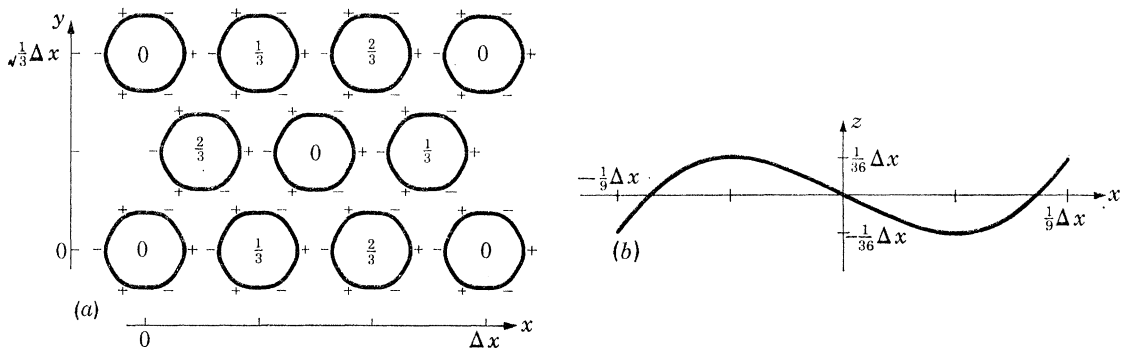

FIGURE 9. The puckered dislocation rings near the z axis, projected on to (*a*) the xy plane and (*b*) the xz plane. The numbers inside the rings on (*a*) give the fractional heights of the centres in the unit cell. Upward and downward puckering is indicated by + and − respectively.

Taking moduli of both sides gives the projections of the dislocations on the xy plane. These projections have the equation

$$\cos(2\sqrt{3}\,\pi y/\Delta x)\{\cos(2\sqrt{3}\,\pi y/\Delta x) + \cos(6\pi x/\Delta x)\} = \tfrac{1}{2}. \tag{5.2}$$

This describes a set of identical rings centred on the lattice points and forming the basis of the dark hexagons. Each ring is almost circular, its radius varying by only about 1 %. The ring centred on $x = y = 0$ attains its greatest radius $r_{\max}$ at the six points where its projection intersects the x axis and directions 60° away (figure 9*a*). From (5.2),

$$r_{\max} = \tfrac{1}{9}\Delta x = 0.1111\Delta x. \tag{5.3}$$

The smallest radius $r_{\min}$ is attained at the six points where the ring intersects the y axis and directions 60° away, and (5.2) gives

$$r_{\min} = (\Delta x/2\pi\sqrt{3})\arccos(\tfrac{1}{2}(\sqrt{3}-1)) = 0.1099\Delta x. \tag{5.4}$$

The height Z of the ring at (x, y) is given by (5.1) as

$$Z = \Delta z\left\{\frac{1}{2\pi}\arg\left(2\exp[6\pi i x/\Delta x]\cos\frac{2\sqrt{3}\,\pi y}{\Delta x} + 1\right) - \frac{2x}{\Delta x}\right\}. \tag{5.5}$$

This equation describes the puckering of the ring, that is, its deviation from a plane curve (figures 8 and 9*b*). Where the radius is $r_{\min}$, $Z = 0$, and the six intersections of the dislocation with this plane can be seen as zeros on figure 7*a*. Where the radius is $r_{\max}$, a little algebra shows that Z is alternately $\pm\frac{1}{36}\Delta z$, the positive value occurring where the ring intersects $+Ox$ and directions 120° away, as can be seen on figure 7*b*. The puckering is sinusoidal to within 3 % of the total depth of the loop.

Downloaded from rsta.royalsocietypublishing.org

Away from the z axis the puckered dislocation rings are tilted relative to planes with constant z. It is the intersection of pairs of such tilted rings off the symmetry axes with the observation plane that gives rise to the dark S shapes visible on figure 2*i*. (S shapes that break the symmetry of the diffraction catastrophe indicate small local deviations in the tilt of the rings.)

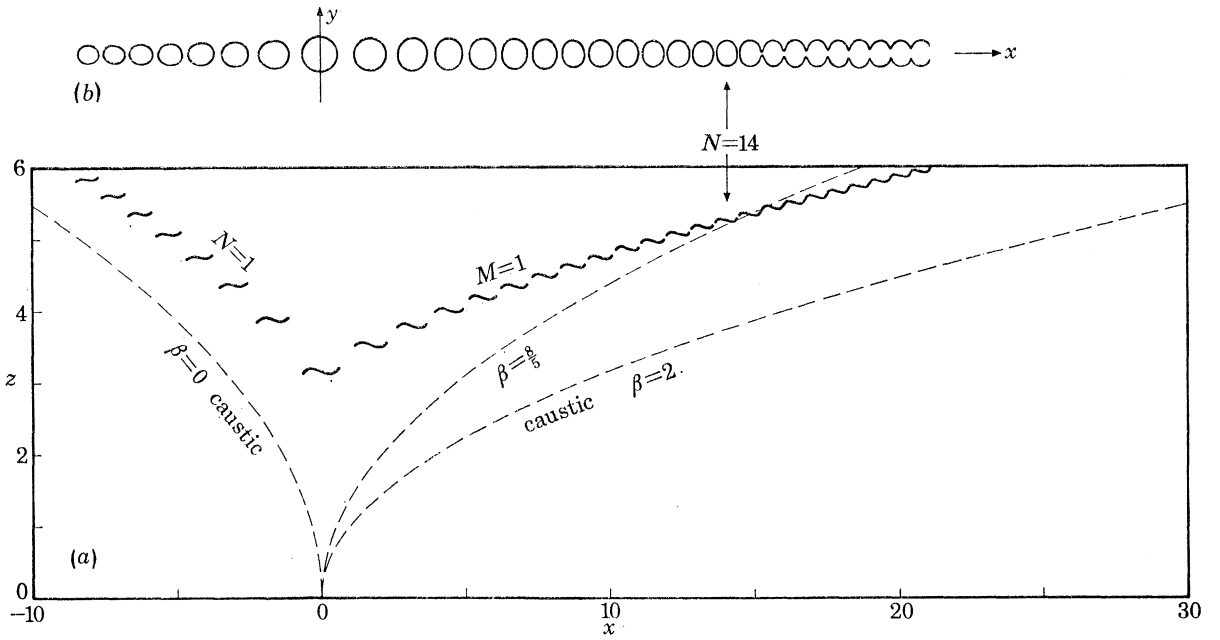

FIGURE 10. Projection of the two sets of dislocations labelled by $M = 1$ and $N = 1$ respectively on to (*a*) the xz plane and (*b*) the xy plane, showing how the rings in the set $M = 1$ join into a hairpin after the ring $N = 14$. The fold, cusp and 'ring-hairpin' lines are shown broken and labelled by their β values of 0, 2 and $\frac{8}{5}$ respectively.

The ring structure just described cannot persist out to the cusps. Consider the vicinity of the cusp at $x = z^2$. Of the four waves, three have high intensity (roots 1, 2 and 4 in (4.17)) and the other is relatively negligible. Therefore the dislocations must be close to those of the Pearcey cusp diffraction pattern, whose dislocations arise from the interference of three waves (appendix C), and take the form of lines parallel to the rib. The lines do not pass through the plane $y = 0$ but consist of pairs disposed on either side of that plane. These line pairs which exist near the rib for large z must change into rings both far from the rib and at small z. As will be shown below, these transitions occur in the following manner. Moving down the Pearcey dislocation lines towards the focus, the influence of the fourth wave gets stronger. This causes the lines to wind helically with increasing amplitude (figure 10 at the right). Eventually the winding is so strong that the lines in a pair meet, thus making a structure resembling a hairpin. Closer to the focus the separate turns of the two helices developed from a line pair have joined together into a row of puckered rings, which approach the z axis in echelon formation (figures 8 and 10*a*) along a close-packed crystallographic direction.

Our first task is to prove the quite general result that a straight dislocation line becomes helical when perturbed by a weak plane wave. In coordinates $(\bar{x}, \bar{y}, \bar{z})$ let the unperturbed wave, with dislocation along $O\bar{z}$, be described by a wave $\psi_0(\bar{x}, \bar{y}, \bar{z})\ e^{-i\omega t}$ which near the $\bar{z}$ axis has the form

$$\psi_0 = B(\bar{x}, \bar{y}) \exp[ik_\parallel \bar{z}] \quad (0 \leqslant |k_\parallel| \leqslant k,\ k = \omega/c = 2\pi/\lambda), \tag{5.6}$$

where

$$B = (a + ic)\bar{x} + (b + id)\bar{y} \tag{5.7}$$

Downloaded from rsta.royalsocietypublishing.org

(cf. Nye & Berry 1974). Therefore B has a first-order zero at $\bar{x} = \bar{y} = 0$ as must be the case for a generic dislocation. Let the perturbing wave be

$$\psi_1 = \epsilon \exp[\mathrm{i}(k_1 \bar{x} + k_2 \bar{y} + k_3 \bar{z})], \tag{5.8}$$

where ϵ is small and positive. The perturbed dislocation satisfies

$$\psi_0 + \psi_1 = 0, \tag{5.9}$$

which can be written as

$$|B(\bar{x}, \bar{y})| = \epsilon, \tag{5.10a}$$

$$\arg B(\bar{x}, \bar{y}) + (k_\parallel - k_3)\bar{z} - (k_1 \bar{x} + k_2 \bar{y}) + \pi = 0. \tag{5.10b}$$

Equation (5.10a), taken together with (5.7), shows that the projection of the dislocation on the $\bar{x}\bar{y}$ plane is an ellipse whose axes have lengths proportional to ϵ. Let us assume, for the moment, that ϵ is sufficiently small for the term $k_1 \bar{x} + k_2 \bar{y}$, namely the phase variation of the perturbing wave across the ellipse, to be negligible. Then equation (5.10b), taken together with the dislocation property of $\arg B$ (namely that $\arg B$ changes by 2π round a circuit enclosing $\bar{x} = \bar{y} = 0$), shows that the ellipse is the axial projection of a helix whose pitch $\delta\bar{z}$ is

$$\delta\bar{z} = 2\pi/|k_\parallel - k_3|. \tag{5.10c}$$

The $\bar{z}$ periodicity $k_\parallel$ of the unperturbed dislocation determines its edge-screw character (Nye & Berry 1974), $k_\parallel = \pm k$ giving a pure screw and $k_\parallel = 0$ giving a pure edge dislocation. The helix arises from beats between the $\bar{z}$ periodicity of the unperturbed dislocation and of the perturbing wave. The largest $\delta\bar{z}$ is infinite, when $k_\parallel = k_3$. The smallest $\delta\bar{z}$, occurring when the unperturbed dislocation is of pure screw type and the perturbing and unperturbed waves travel in opposite directions, so that $k_\parallel = k = 2\pi/\lambda$ and $k_3 = -k$, is

$$\delta\bar{z} = \frac{2\pi}{2k} = \tfrac{1}{2}\lambda.$$

In the present problem the unperturbed dislocations are those of the Pearcey pattern, and the perturbing locally plane wave is the fourth ray contribution to the elliptic umbilic catastrophe. Therefore the Pearcey lines are indeed perturbed into helices as we asserted.

There is, however, a further aspect to be considered, which causes the asymptotic form of these helices to be curiously complicated. As we follow a dislocation (one arm of a hairpin) outwards it is true that the perturbing ray gets weaker, but at the same time it makes a larger angle with the axis of the helix. This means that the phase variation $k_1 \bar{x} + k_2 \bar{y}$ of the fourth wave perpendicular to the axis of the helix is no longer negligible, even though ϵ is smaller. The effect of the term $k_1 \bar{x} + k_2 \bar{y}$ in equation (5.10b) is to shear the helix parallel to its axis, and this can in fact be seen in figure 10a. Further out still, the shearing is so great that a given turn of the helix can cut a plane perpendicular to the helix axis more than once (always an odd number of times); but, however great the shearing, the dislocation always remains a single continuous line. Examples of these multiple intersections, clustered round ellipses centred on the zeros of the Pearcey pattern, can be seen on figure 4 (there are several outside the caustic). When considering the problem of how these sheared helices turn asymptotically into the unperturbed dislocation lines of the Pearcey pattern it is simpler to work in the space of natural dimensionless coordinates (x, y, z), rather than in the physical space (x', y', z'). We show in appendix D that for large values of a coordinate s in (x, y, z) space, measuring arc length along the helix axis (i.e. parallel to the rib), the asymptotic behaviour of the dislocation helices is as follows: the width of the helix in the plane

Downloaded from rsta.royalsocietypublishing.org

parallel to the plane of the rib (i.e. in the xz plane for dislocations associated with the rib at $y = 0$) decreases as $s^{-\frac{5}{8}}$, and the width of the helix perpendicular to this plane decreases as $s^{-\frac{1}{2}}$; the number of intersections of the helix with a plane perpendicular to its axis (which measures the degree of shearing) increases as $s^{\frac{3}{8}}$; the pitch of the helix decreases as $s^{-\frac{1}{2}}$. In the limit, then, the dislocation winds infinitely rapidly round an infinitely thin flat narrow 'ribbon' and is infinitely sheared. Because successive intersections with a plane perpendicular to the axis are of opposite strength the net effect of the large odd number of intersections is of a single straight dislocation line. The approach to the limit is, however, unprecedented.

To examine the transition from rings to hairpins we use the analytical four-wave theory in the xz plane developed in § 4 and embodied in the expression (4.18) for $E(x, 0, z)$. We seek the zero points of this expression, which will tell us where dislocation lines cross the xz plane. It is convenient to define

$$\left.\begin{aligned} \zeta &\equiv \tfrac{1}{3}z^3, \\ \beta &\equiv \sqrt{(1+3x/z^2)}, \end{aligned}\right\} \tag{5.13}$$

so that β runs from 0 through 1 to 2 as x runs from $-\frac{1}{3}z^2$ (fold) through 0 (centre of pattern) to z^2 (rib). Then the zeros of (4.18) are points in the ζ, β plane satisfying

$$2\sqrt{\left(\frac{\beta}{2+\beta}\right)}\exp\left[-\mathrm{i}\{\zeta(\tfrac{2}{3}\beta^3-2\beta^2+\tfrac{8}{3})+\tfrac{1}{2}\pi\}\right]+\sqrt{\left(\frac{2-\beta}{2+\beta}\right)}\exp\left[-\mathrm{i}\{\tfrac{4}{3}\zeta\beta^3+\tfrac{1}{2}\pi\}\right]-1=0. \tag{5.14}$$

The moduli of the three terms in this equation must satisfy the triangle inequalities. Two of these are always satisfied for $0 \leqslant \beta \leqslant 2$, but the third, namely

$$\sqrt{\left(\frac{2-\beta}{2+\beta}\right)}+1 \geqslant 2\sqrt{\left(\frac{\beta}{2+\beta}\right)}, \tag{5.15}$$

yields the non-trivial restriction

$$\beta \leqslant \tfrac{8}{5}. \tag{5.16}$$

In terms of the original variables (5.13) this means that all dislocation crossings of the plane $y = 0$ must satisfy

$$x \leqslant \tfrac{13}{25}z^2. \tag{5.17}$$

The parabola $x = \frac{13}{25}z^2$ is indicated on figure 10*a* (dashed line, $\beta = \frac{8}{5}$). It marks the transition from rings to hairpins, since the solutions of (5.14) correspond to rings intersecting the xz plane.

Some algebra shows that the solutions of (5.14) fall into two families, A and B; within each family the roots, labelled by M and N, are the intersections of curves $\zeta_M(\beta)$ and $\zeta_N(\beta)$ whose equations are

$$\left.\begin{aligned} \zeta_{MA}(\beta) &= \frac{3}{2\beta^3-6\beta^2+8}\left\{2M\pi-\arcsin\frac{3}{2}\sqrt{\left(\frac{\beta}{2+\beta}\right)}\right\}, \\ \zeta_{NA}(\beta) &= \frac{3}{4\beta^3}\left\{(2N-1)\,\pi-\arcsin\frac{2(\beta-1)}{\sqrt{(4-\beta^2)}}\right\}; \end{aligned}\right\} \tag{5.18a}$$

$$\left.\begin{aligned} \zeta_{MB}(\beta) &= \frac{3}{2\beta^3-6\beta^2+8}\left\{(2M-1)\,\pi+\arcsin\frac{3}{2}\sqrt{\left(\frac{\beta}{2+\beta}\right)}\right\}, \\ \zeta_{NB}(\beta) &= \frac{3}{4\beta^3}\left\{2N\pi+\arcsin\frac{2(\beta-1)}{\sqrt{(4-\beta^2)}}\right\}; \end{aligned}\right\} \tag{5.18b}$$

$$(M, N = 1, 2, 3, \ldots).$$

The two sets of A curves were plotted, and their intersections read off and replotted on the original xz plane; the corresponding exercise was carried out for the B curves. The resulting

Downloaded from rsta.royalsocietypublishing.org

dislocation points form the ends of all the dislocation projections inside the caustic in figure 8; their positions are indistinguishable from those shown on figure 5*b* computed exactly from the diffraction integral.

The integers M and N in (5.18) have the following meaning. Fixing M and N defines a puckered dislocation ring; the A root corresponds to the left hand intersection of the ring with $y = 0$ and the B root corresponds to the right hand intersection. Each value of M corresponds to a close-packed row of dislocation rings, with N labelling rings in the row. Rings encircling the z axis have $M = N$. Figure 10*a* shows projections on to the xz plane of the rows $M = 1$ and $N = 1$ of dislocation rings, and figure 10*b* shows the projection of these rings on to the xy plane. (These projections were computed using the method of stationary phase in the xz plane, extended to small y by perturbation theory.) The projections for other values of M and N were sketched between their previously computed end points on figure 8.

It is evident that along a close packed row as N increases and the limiting line $\beta = \frac{8}{5}$ is approached the separation of the rings decreases. Moreover, we recall from figure 9*a* that neighbouring rings pucker towards one another. In each row there is a last ring with $N = N_{\max}(M)$, just before the transition to a hairpin. To find $N_{\max}(M)$, imagine that, for a given M, equations (5.18) had a B type solution on the limiting parabola $\beta = \frac{8}{5}$, corresponding to some value of N. Then inspection shows that this would coincide with an A root corresponding to $N+1$: the last ring would touch the bend of the hairpin. In fact this is an infinitely improbable occurrence, since solving (5.18*a*) with $\beta = \frac{8}{5}$ and $\zeta_M = \zeta_N$ gives a non-integral value of N. However, the integer part of this N-value gives the last B root occurring for the given M, and this is just $N_{\max}(M)$. Elementary calculation then gives

$$N_{\max}(M) = \text{integer part of } \left(\frac{512}{27}M - \frac{539}{104}\right). \tag{5.19}$$

Beyond the last B root, with $N = N_{\max}(M)$, and very close to $\beta = \frac{8}{5}$, there is a last A root with $N = N_{\max}(M)+1$. This is the left hand side of a ring that never gets completed; in fact it is the bend of the hairpin. For $M = 1$, equation (5.19) gives $N_{\max}(1) = 14$, which is therefore the number of rings in the first row. The corresponding value of z is 5.348. These predictions can be verified by inspection of figures 8 or 10. For $M = 2$, $N_{\max}(2) = 34$ and $z = 7.093$.

Our final topic is the study of dislocations outside the caustic. First there is an array of dislocations lying entirely in the plane $z = 0$. These are the black lines in figure 3*a*. The region of low amplitude associated with each dislocation is greatly elongated in the z direction: it is still visible with little change at $z = 6$. In addition to these dislocations, far from the focus and close to the rib there are the lines of the Pearcey pattern (appendix C) perturbed into sheared helices as explained earlier. What happens as these helices approach the focus? It proved very difficult to answer this question on the basis of an analytic study of $E(x, y, z)$ using stationary-phase methods, for two reasons: first, because one of the rays contributing to interference leading to dislocations outside the rib is complex (appendix C) and this makes the analysis impenetrably elaborate; and second, because these dislocations sometimes get so close to the caustic that the ordinary method of stationary phase breaks down. Therefore the description that follows is based on direct computations of the diffraction integral for $E(x, y, z)$.

There is an infinite sequence of helices (figure 11*a*) lying close to the fold caustic surface, and roughly parallel to a rib. As a helix approaches the focus its radius gets larger as the perturbing wave gets relatively stronger, but since these helices do not occur as distinct pairs (appendix C)

Downloaded from rsta.royalsocietypublishing.org

they cannot break up into rings like those inside the caustic. Instead each helix eventually crosses the symmetry plane between two ribs where it joins up smoothly with the similar helix (of opposite hand) originating from the next rib. The result can be regarded as a sort of hairpin whose arms have been forced apart, but it more closely resembles a pair of joined curly antelope's horns. Figures 11*b* and 11*c* shows projections on to the *xz* and *yz* planes of the parts of the first three of these dislocations nearest to the focus.

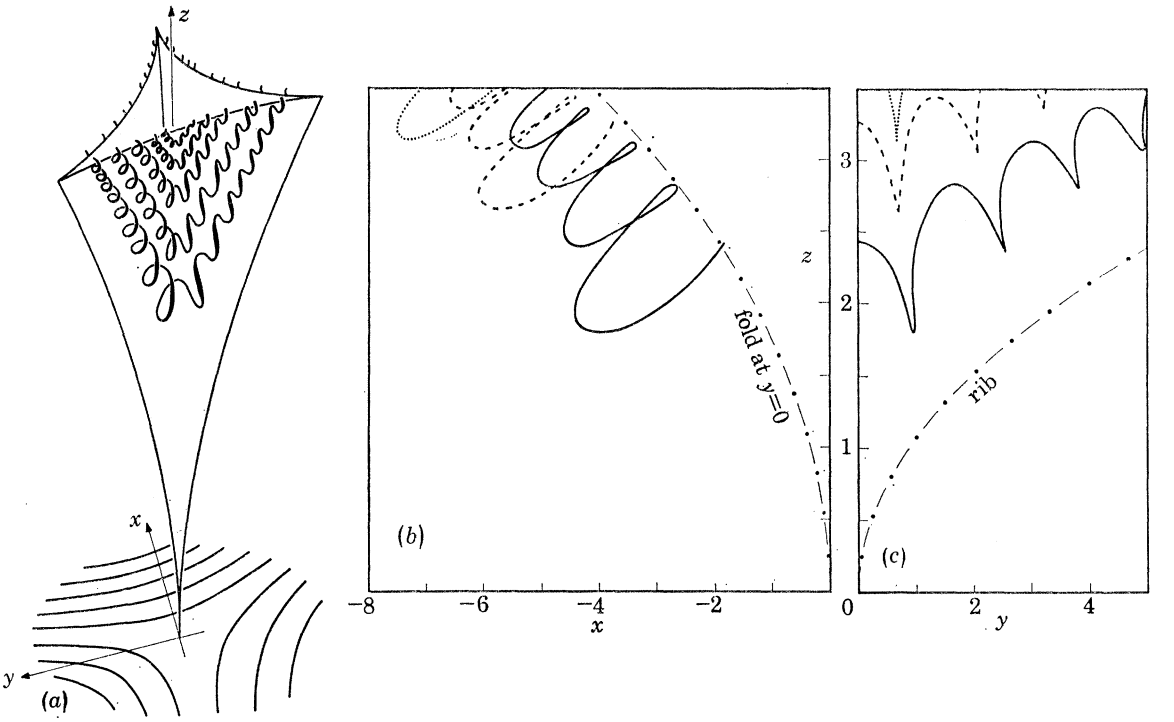

FIGURE 11. (*a*) The three-dimensional configuration of the dislocation lines outside the caustic for $z \geqslant 0$ (rough sketch only). The set of helical dislocation lines fully visible are shown accurately in projection in (*b*) and (*c*). (*b*) Projection of parts of three of the dislocation lines outside the caustic nearest to the focus on to the *xz* plane. The intersection of the caustic with this plane is shown as a chain line. (*c*) Projection on to the *yz* plane.

6. Discussion

The main result of this study has been the discovery and explanation of a surprising richness of diffraction detail decorating the comparatively simple elliptic umbilic caustic surface. In our model system we have been able to use equations which are valid both near and far from the focus. However, in a more general system where there is an elliptic umbilic focus, catastrophe theory describes only the *local* structure of the geometrical optics caustic near the focus. In a similar way our wave theory in that case gives the *local* diffraction structure. In any given experimental situation the scale of this structure will be large or small depending on the wavelength, and this means that one will not necessarily observe the whole of the calculated structure: for example, the outer parts may be associated with a part of the caustic that is being affected by another nearby catastrophe. But this does not mean that the outer details of the calculated pattern have no general significance. On the contrary, as the wavelength approaches zero, all details flow in towards the focus and so any given detail can be made 'local' by choosing λ sufficiently small. It is this local diffraction pattern that we have calculated.

Downloaded from rsta.royalsocietypublishing.org

The reason for expending so much effort elucidating its structure is that all elliptic umbilic diffraction catastrophes are alike: they have the important property, which they share with all diffraction catastrophes, of being *structurally stable* against perturbation, in the following sense. Imagine the diffraction pattern to be embedded in rubber; then if the initial wavefront, or the medium through which the wave is propagating, is slightly changed the perturbed pattern can be obtained from the original one by smooth deformation of the rubber (i.e. stretching or compressing without tearing). This stability property explains why diffraction catastrophes occur in short-wave optics whenever no continuous symmetries are present, for example in waves refracted by irregular glass surfaces (Berry 1976) or irregular water droplet lenses (Nye 1978). The pattern whose stability is asserted here is that associated with the intensity $|E|^2$ or modulus $|E|$. The phase patterns, on the other hand, can be very varied, corresponding to waves ψ in which E is multiplied by different phase factors (one example of which occurs in equation (2.6)). This variation is not completely arbitrary, however, since the singularities of phase – the dislocations – must lie along the zeroes of $|E|$.

At the relatively coarse level of geometrical optics the stability of the elliptic umbilic caustic surface is guaranteed by catastrophe theory (Poston & Stewart 1978). The structural stability of the diffraction catastrophe is, however, a much stronger property, and moreover a useful one (it was implicitly invoked by Nye (1978) who identified the singular section of the elliptic umbilic caustic from irregular droplets by the diffraction 'star' shown on figure 2*a*). Even the dislocation lines – the most delicate features of the diffraction pattern – are structurally stable.

To see that this is the case, consider the lattice of puckered dislocation rings (§ 5) near the symmetry axis far from the focus. On the simplest theory the rings result from the interference of four plane waves. But the waves are not really plane, and an exact four-wave theory based on the method of stationary phase shows that the lattice is distorted; the dislocation rings survive the perturbation associated with this increase in sophistication. However, the method of stationary phase is itself an approximation to the diffraction integral (1.7), and computation shows that the rings survive this further perturbation. Finally, the diffraction integral is only an approximation to any experiment such as that described in § 2, but still the rings survive even when perturbations break the symmetry of the standard catastrophe (as shown by some of the dark S shapes on figure 2*i*).

It is evident, then, that the dislocation rings are stable. However, the structural stability of the dislocation lines associated with the cusp diffraction catastrophes (appendix C) far from the focus is less straightforward. In the elliptic umbilic diffraction catastrophe the lines are perturbed into helices as explained in § 5, but the helices approach the cusp dislocation lines in a surprisingly complicated fashion, winding ever more tightly and shearing ever more strongly. Moreover the analysis in appendix D indicates that this strange asymptotic behaviour will occur more generally, whenever a dislocation associated with any diffraction catastrophe is perturbed by a locally plane wave (or a wave associated with a less singular catastrophe). Nevertheless such a dislocation *is* structurally stable, because its helix remains one continuous curve, albeit a complicated one. (It is worth remarking that no crystal dislocation could exhibit this behaviour, on account of the smoothing effect of its line tension.)

Dislocations outside the caustic (§ 5 and appendix C) have the interesting feature that they are produced by interference between a complex ray and one or more real rays. This is the only case we know of where complex rays affect the topology of a wave field.

It is clear that each diffraction catastrophe will have its characteristic architecture, and

Downloaded from rsta.royalsocietypublishing.org

consideration of our work on the elliptic umbilic together with previous studies of diffraction near the fold (Airy pattern) and the cusp (Pearcey pattern) strongly suggests that the architecture will increase in complexity very rapidly with increasing codimension. In addition to the elliptic umbilic there are two more catastrophes with codimension three, namely the swallowtail and the hyperbolic umbilic, and we have begun a detailed study of their associated diffraction. Exploration of the higher diffraction catastrophes provides seemingly inexhaustible opportunities for further experimental and theoretical research.

We should like to thank the staff of Bristol University Computer Centre for their help and advice; Mr S. Godden of the Department of Geography for tracing the more complicated contour plots; and Mr G. Keene for photographic assistance. One of us (F.J.W.) would like to acknowledge the financial support of the S.R.C.

Appendix A. Edge diffraction effects

In (2.2) the domain of integration was the illuminated triangular aperture in the $\xi'\eta'$ plane, but in deriving the diffraction catastrophe formula (2.6) the domain was extended so as to include the whole $\xi'\eta'$ plane. This introduced an error equivalent to neglecting a wave ψ' given by an integral like (2.2) with the sign changed and the domain restricted to the region *outside* the aperture. We are interested in observation points x', y', z' near the elliptic umbilic focus, for which the integrand in ψ' has no stationary points. This implies that for small λ the dominant contributions come from the boundary of the domain of integration, that is, from the perimeter of the droplet, so that ψ' is indeed an edge wave. Moreover, near the focus it is permissible to consider ψ' as the sum of three separate contributions from each of the edges, regarded as infinitely long; this implies neglect of corner waves, which must be of higher order in λ. Therefore we shall work out the strength and scale of the three edge contributions to ψ' and show them to be negligible in comparison with the diffraction catastrophe (2.6).

Interference of these three waves near the focus produces a pattern varying much faster in the x', y' planes than in the z' direction, so that z' will henceforth be set equal to the focal value (2.8). Only the contribution ψ_e from the edge $\xi' = -\frac{1}{2\sqrt{3}}L$ (a zero contour of (2.4)) need be evaluated, since the other two waves are related to this by symmetry. From (2.2), ψ_e is given by

$$\psi_e(x', y', z') \approx \frac{\psi_0 e^{i\alpha}}{\lambda z'} \int_{-\infty}^{-L/2\sqrt{3}} d\xi' \int_{-\infty}^{\infty} d\eta' \exp\left[2\pi i\{(\mu-1)h(\xi', \eta') + \tfrac{1}{2}(\xi'^2+\eta'^2)/z' - x'\xi'/z' - y'\eta'/z'\}/\lambda\right], \quad (A\,1)$$

where α is an irrelevant phase (that will change its meaning as the calculation proceeds) and $h(\xi', \eta')$ is the droplet height profile (2.4). The η' integration can be performed exactly, and gives

$$\psi_e(x', y', z') \approx \frac{\psi_0 e^{i\alpha}}{\lambda z'} \left(\frac{\lambda L^2}{18H(\mu-1)}\right)^{\frac{1}{2}} \times \int_{-\infty}^{-L/2\sqrt{3}} d\xi' \exp\left[2\pi i\{\tfrac{9}{2\sqrt{3}}y'^2 H(\mu-1)/L\xi' + 6\sqrt{3}H(\mu-1)\,\xi'^3/L^3 + \tfrac{1}{2}\xi'^2/z' - x'\xi'/z'\}/\lambda\right]. \quad (A\,2)$$

(It is worth remarking that the length of edge contributing substantially to the η' integral was of order $L\sqrt{(\lambda/H(\mu-1))}$, which is much smaller than L, confirming our expectation that the corners give negligible contribution.)

Downloaded from rsta.royalsocietypublishing.org

The dominant contribution to (A 2) comes from the upper limit of integration, and integration by parts (Dingle 1973) leads to

$$\psi_e(x', y', z' = \tfrac{1}{18}L^2/H(\mu-1)) \approx \frac{\psi_0 \, e^{i\alpha}\lambda^{\frac{1}{2}}L^2}{9\pi\sqrt{6}[H(\mu-1)]^{\frac{3}{2}}z'} \exp\left[2\pi i\{3\sqrt{3H(\mu-1)}\,x'/L\}/\lambda\right], \quad (A\,3)$$

where only the term of lowest order in x' has been explicitly retained in the phase. The total edge wave near the focus is the sum of three terms like (A 3), and we now compare its strength and scale with the diffraction catastrophe (2.6).

At the focus itself the amplitude ratio r of the three edge waves to the diffraction catastrophe is

$$r \equiv \frac{3\psi_e(0, 0, z' = \frac{1}{18}L^2/H(\mu-1))}{\psi(0, 0, z' = \frac{1}{18}L^2/H(\mu-1))} = \left(\frac{\lambda}{H(\mu-1)}\right)^{\frac{5}{6}} \frac{12\pi\sqrt{3}}{9\sqrt{(6\pi)}\,\Gamma(\frac{7}{6})} = 1.4\left(\frac{\lambda}{H(\mu-1)}\right)^{\frac{5}{6}}. \quad (A\,4)$$

This is small whenever the droplet lens changes the phase of the incident wave by a large amount. Under these circumstances the edge wave and the diffraction catastrophe can be considered separately and our approximations are justified. If H gets small enough (as the droplet evaporates, for example) for r to be of order unity it is no longer possible to effect the separation between the edge wave and the catastrophe; the extreme case is $r = \infty$ ($H = 0$) when there is no droplet at all and the problem reduces to ordinary diffraction from an aperture. In our experiment a typical value of H is 0.1 mm, and then (A 4) gives $r = 0.05$, so that the intensity of the edge wave is only 0.25 % of that of the catastrophe at focus. The edge waves produce their greatest effect on the elliptic umbilic dislocations, which according to the arguments in § 5 will be perturbed into helices winding round those contour 'tubes' for which $|E(x, y, z)/E(0, 0, 0)| = r$. For $r = 0.05$ these tubes are negligibly thin on the scale of figures 2 and 3, so that the edge waves are of no importance in this experiment.

To estimate the scale of the edge waves' interference pattern it suffices to consider the x' variation in (A 3). This shows that the edge wave fringes $\Delta x'_e$ have a scale

$$\Delta x'_e = \tfrac{1}{3\sqrt{3}}\lambda L/H(\mu-1), \quad (A\,5)$$

which should be compared with the catastrophe fringe scale $\Delta x'$ given by (4.11) and (4.10). The scale ratio ρ at the height z_n (equation (4.4)) of the nth lattice 'plane' is

$$\rho \equiv \Delta x'_e/\Delta x' = 0.28 z_n\{\lambda/H(\mu-1)\}^{\frac{1}{3}}. \quad (A\,6)$$

For $H = 0.1$ mm, $\rho = 0.07 z_n$, which becomes comparable with unity only at the lattice plane $n \approx 60$; this is far outside the range studied in our experiment, so that edge wave fringes are so close together as to be negligible in scale as well as strength.

Appendix B. Series expansion for $E(x, y, z)$

Here we derive an expansion in powers of z for the fundamental diffraction integral (1.7) for $E(x, y, z)$, whose first term $E(x, y, 0)$ is the simple closed form (3.4).

It is convenient first to study the closely related diffraction integral for the hyperbolic umbilic, namely

$$H(x, y, z) = \frac{1}{2\pi}\int\int_{-\infty}^{\infty} d\xi\, d\eta \exp\left[i\{\xi^3 + \eta^3 + z\xi\eta - x\xi - y\eta\}\right] \quad (B\,1)$$

(Duistermaat 1974; Berry 1976). Rotation of coordinates in the $\xi\eta$ plane by $\frac{1}{4}\pi$ and scaling by a factor $2^{\frac{1}{3}}$ gives

$$H(x, y, z) = \frac{2^{\frac{1}{3}}}{2\pi}\int\int_{-\infty}^{\infty} d\xi\, d\eta \exp\left[i\{\xi^3 + 3\xi\eta^2 + z(\xi^2 - \eta^2)/2^{\frac{2}{3}} - (x+y)\,\xi/2^{\frac{1}{3}} - (-x+y)\,\eta/2^{\frac{1}{3}}\}\right]. \quad (B\,2)$$

Downloaded from rsta.royalsocietypublishing.org

In this expression the only significant difference from the elliptic umbilic diffraction catastrophe (1.7) is the sign of η^2. Therefore it is sensible to seek a transformation of (1.7), considered as a double contour integral in the two complex ξ and η planes, that enables E to be expressed in terms of H. Then the required series expansion for E will be obtained from that for H. We get this from (B 1) by expanding the exp $(iz\xi\eta)$ factor in powers of z, which yields

$$H(x,y,z) = \frac{2\pi}{3^{\frac{2}{3}}} \sum_{n=0}^{\infty} \frac{(-i3^{-\frac{2}{3}}z)^n}{n!} \mathrm{Ai}^{(n)}\left(\frac{-x}{3^{\frac{1}{3}}}\right) \mathrm{Ai}^{(n)}\left(\frac{-y}{3^{\frac{1}{3}}}\right), \tag{B 3}$$

where

$$\mathrm{Ai}^{(n)}(s) \equiv \frac{\mathrm{d}^n \mathrm{Ai}(s)}{\mathrm{d}s^n} \tag{B 4}$$

and $\mathrm{Ai}(s)$ is the ordinary Airy function (Abramowitz & Stegun 1964) defined as

$$\mathrm{Ai}(s) \equiv \frac{1}{2\pi} \int_{-\infty}^{\infty} \mathrm{d}t \exp\left[i(\tfrac{1}{3}t^3 + st)\right]. \tag{B 5}$$

Let C_ξ and C_η denote the contours of integration in (1.7); initially C_ξ is the real ξ axis and C_η the real η axis. The obvious transformation to change the sign of η^2 is simply rotation of C_η by $\pm\frac{1}{2}\pi$ but this fails because the η integral diverges during the rotation. In fact we accomplish the sign reversal of η^2 in terms of *two* transformations, + and −, defined as follows:

$$C_\xi^{\pm} = C_\xi \quad \text{rotated by} \quad \pm\tfrac{2}{3}\pi,$$
$$C_\eta^{\pm} = C_\eta \quad \text{rotated by} \quad \pm\tfrac{1}{6}\pi.$$

By deforming C_ξ as shown on figure 12, into $-C_\xi^+ - C_\xi^-$ together with an arc at infinity whose contribution is zero, the double integral (1.7) splits into two integrals, that can be written in an obvious notation as

$$E(x,y,z) = \int_{-\infty}^{\infty} \mathrm{d}\xi \int_{-\infty}^{\infty} \mathrm{d}\eta = -\int_{C_\xi^+} \mathrm{d}\xi \int_{C_\eta^+} \mathrm{d}\eta - \int_{C_\xi^-} \mathrm{d}\xi \int_{C_\eta^-} \mathrm{d}\eta. \tag{B 6}$$

Explicitly, this is

$$\begin{aligned} E(x,y,z) = &-\frac{\mathrm{e}^{+\frac{5}{6}i\pi}}{2\pi} \int_{-\infty}^{\infty} \mathrm{d}\xi \int_{-\infty}^{\infty} \mathrm{d}\eta \exp\left[i\{\xi^3 + 3\xi\eta^2 + z\,\mathrm{e}^{\frac{1}{3}i\pi}(\xi^2 - \eta^2) - x\,\mathrm{e}^{\frac{2}{3}i\pi}\xi - y\,\mathrm{e}^{\frac{1}{6}i\pi}\eta\}\right] \\ &-\frac{\mathrm{e}^{-\frac{5}{6}i\pi}}{2\pi} \int_{-\infty}^{\infty} \mathrm{d}\xi \int_{-\infty}^{\infty} \mathrm{d}\eta \exp\left[i\{\xi^3 + 3\xi\eta^2 + z\,\mathrm{e}^{-\frac{1}{3}i\pi}(\xi^2 - \eta^2) - x\,\mathrm{e}^{-\frac{2}{3}i\pi}\xi - y\,\mathrm{e}^{-\frac{1}{6}i\pi}\eta\}\right]. \end{aligned} \tag{B 7}$$

By comparison with (B 2) this can now be expressed in terms of H as

$$E(x,y,z) = 2^{-\frac{1}{3}}\{\mathrm{e}^{-\frac{1}{6}i\pi} H(X,Y,Z) + \mathrm{e}^{\frac{1}{6}i\pi} H(X^*, Y^*, Z^*)\}, \tag{B 8}$$

where

$$\left.\begin{aligned} X &= 2^{-\frac{2}{3}}\,\mathrm{e}^{\frac{2}{3}i\pi}(x + iy), \\ Y &= 2^{-\frac{2}{3}}\,\mathrm{e}^{\frac{2}{3}i\pi}(x - iy), \\ Z &= 2^{\frac{2}{3}}\,\mathrm{e}^{\frac{1}{3}i\pi} z. \end{aligned}\right\} \tag{B 9}$$

Now the series expansion for E can be obtained by using (B 3) as

$$E(x,y,z) = (\tfrac{2}{3})^{\frac{2}{3}}\pi \sum_{n=0}^{\infty} \left\{\mathrm{e}^{-\frac{1}{6}i\pi} \frac{(iu)^n}{n!} \mathrm{Ai}^{(n)}(\mathrm{e}^{\frac{2}{3}i\pi}v)\, \mathrm{Ai}^{(n)}(\mathrm{e}^{\frac{2}{3}i\pi}v^*) + \mathrm{e}^{\frac{1}{6}i\pi} \frac{(iu^*)^n}{n!} \mathrm{Ai}^{(n)}(\mathrm{e}^{-\frac{2}{3}i\pi}v^*)\, \mathrm{Ai}^{(n)}(\mathrm{e}^{-\frac{2}{3}i\pi}v)\right\}, \tag{B 10}$$

where

$$\left.\begin{aligned} u &\equiv -(\tfrac{2}{3})^{\frac{2}{3}}\,\mathrm{e}^{\frac{1}{3}i\pi} z, \\ v &\equiv -12^{-\frac{1}{3}}(x + iy). \end{aligned}\right\} \tag{B 11}$$

Downloaded from rsta.royalsocietypublishing.org

In the plane $z = 0$ this series reduces to its first term, which may be simplified using the relation

$$\mathrm{Ai}(\mathrm{e}^{\pm\frac{2}{3}\mathrm{i}\pi}v) = \tfrac{1}{2}\,\mathrm{e}^{\pm\frac{1}{3}\mathrm{i}\pi}\{\mathrm{Ai}(v) \mp \mathrm{iBi}(v)\}. \tag{B 12}$$

(Abramowitz & Stegun 1964), where Bi denotes the second standard solution of Airy's equation. Then the first term of (B 10) becomes

$$E(x, y, 0) = (\tfrac{2}{3})^{\frac{2}{3}}\,\tfrac{1}{2}\pi\{\mathrm{Ai}(v)\,\mathrm{Bi}(v^*) + \mathrm{Ai}(v^*)\,\mathrm{Bi}(v)\}, \tag{B 13}$$

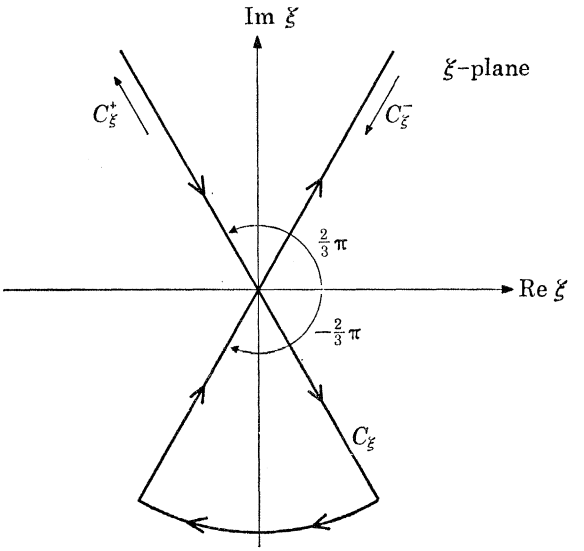

FIGURE 12. Integration contour in ξ plane.

which is the expression (3.4) that we set out to derive. This result shows that $E(x, y, 0)$ is real and invariant under the transformation $y \to -y$. The threefold rotation symmetry is, however, not obvious. It can be made so with the aid of a relation analogous to (B 12), namely

$$\mathrm{Bi}\,(\mathrm{e}^{\pm\frac{2}{3}\mathrm{i}\pi}v) = \tfrac{1}{2}\,\mathrm{e}^{\mp\frac{1}{6}\mathrm{i}\pi}\{3\,\mathrm{Ai}(v) \pm \mathrm{i}\,\mathrm{Bi}(v)\}, \tag{B 14}$$

which when employed in (B 13) gives the form

$$E(x, y, 0) = (\tfrac{2}{3})^{\frac{2}{3}}\,\tfrac{1}{3}\pi\{\mathrm{Ai}(v)\,\mathrm{Bi}^*(v) + \mathrm{Ai}(\mathrm{e}^{\frac{2}{3}\mathrm{i}\pi}v)\,\mathrm{Bi}^*(e^{\frac{2}{3}\mathrm{i}\pi}v) + \mathrm{Ai}\,(\mathrm{e}^{-\frac{2}{3}\mathrm{i}\pi}v)\,\mathrm{Bi}^*\,(\mathrm{e}^{-\frac{2}{3}\mathrm{i}\pi}v)\} \tag{B 15}$$

in which the rotation symmetry is manifest since rotations in xy are equivalent to rotations in the complex v plane.

An immediate application of the series (B 10) is to express E on the z axis near the focus as

$$E(0, 0, z) = (\tfrac{2}{3})^{\frac{2}{3}}\,\pi\sqrt{3}\{(\mathrm{Ai}\,(0))^2 - \mathrm{i}(\tfrac{2}{3})^{\frac{2}{3}}\,(\mathrm{Ai}^{(1)}(0))^2 z + O(z^3)\}. \tag{B 16}$$

This shows what is obvious from figure 5*a*, that the maximum intensity occurs not at the elliptic umbilic focus but at points above and below it.

Finally, note that our evaluation of E in the plane $z = 0$ implies the following non-trivial Fourier transform of the Airy function:

$$\frac{1}{2\pi}\int_{-\infty}^{\infty} \mathrm{d}x\,\mathrm{Ai}\,(a - x^2)\,\mathrm{e}^{\mathrm{i}bx} = 2^{-\frac{1}{3}}\,\mathrm{Re}\left\{\mathrm{Ai}\left(\frac{a + \mathrm{i}b}{2^{\frac{2}{3}}}\right)\,\mathrm{Bi}\left(\frac{a - \mathrm{i}b}{2^{\frac{2}{3}}}\right)\right\}, \tag{B 17}$$

as well as its simpler companion

$$\frac{1}{2\pi}\int_{-\infty}^{\infty} \mathrm{d}x\,\mathrm{Ai}\,(a + x^2)\,\mathrm{e}^{\mathrm{i}bx} = 2^{-\frac{1}{3}}\,\mathrm{Ai}\left(\frac{a + b}{2^{\frac{2}{3}}}\right)\,\mathrm{Ai}\left(\frac{a - b}{2^{\frac{2}{3}}}\right). \tag{B 18}$$

Downloaded from rsta.royalsocietypublishing.org

Appendix C. Three-wave theory for the cusp diffraction catastrophe

Our purpose here is to describe the cusp diffraction catastrophe and to assess the accuracy of the stationary-phase approximation to its defining integral. In a way this appendix is a microcosm of the whole paper, and our results here give confidence in the accuracy of the more complicated but conceptually similar approximations for the elliptic umbilic catastrophe. The cusp integral is

$$C(x,y) = \frac{1}{\sqrt{(2\pi)}}\int_{-\infty}^{\infty} \mathrm{d}\xi \exp\left[\mathrm{i}(\tfrac{1}{4}\xi^4 + \tfrac{1}{2}x\xi^2 + y\xi)\right] \qquad (\mathrm{C}\,1)$$

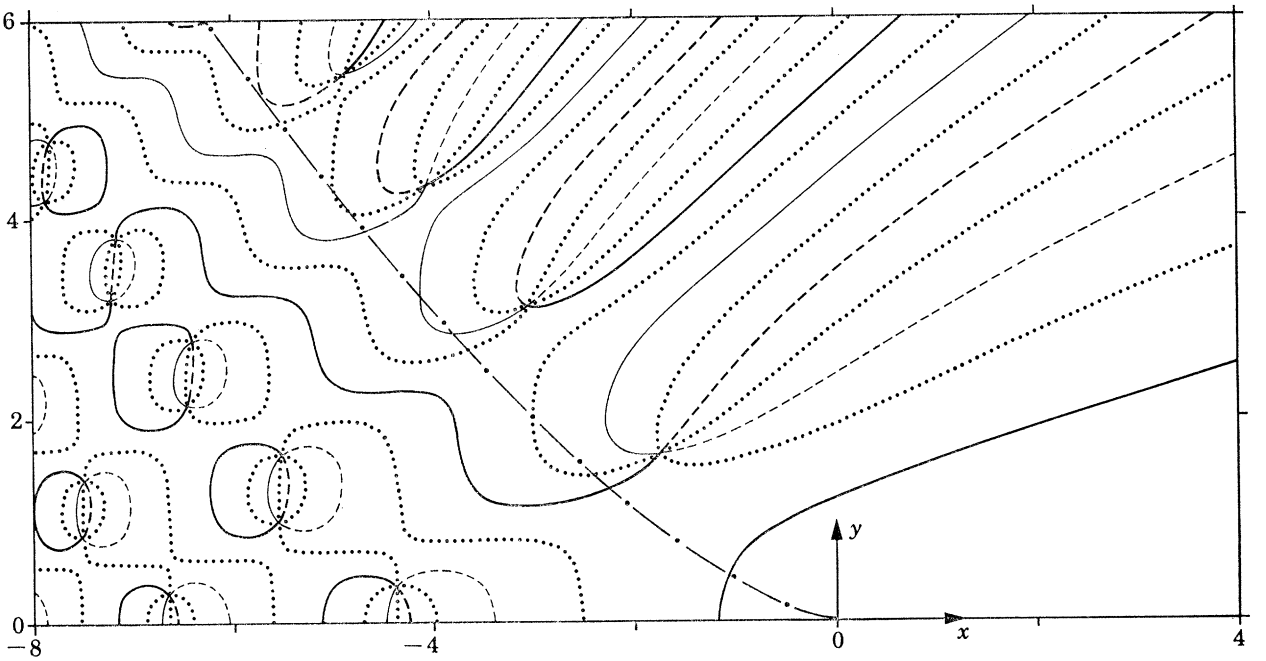

Figure 14. Equiphase lines of $C(x,y)$; the caustic is represented by a chain line.
—— 0; —— $\frac{1}{2}\pi$; – – – π; – – – $-\frac{1}{2}\pi$; ..... $\pm\frac{1}{4}\pi$, $\pm\frac{3}{4}\pi$.

and was first studied in numerical detail by Pearcey (1946). It is easy to show by the methods employed in § 1 for the elliptic umbilic that the cusped caustic has the equation

$$y^2 + \tfrac{4}{27}x^3 = 0. \qquad (\mathrm{C}\,2)$$

The function $C(x,y)$ decorates this with diffraction detail.

Figures 13*a* and *b* (plate 4) show photographs of the cusp diffraction catastrophe, produced in the near field of a parallel beam of laser light that has passed horizontally through a water droplet lens lying in a V-shaped aperture in adhesive tape stuck on to a vertical microscope slide. For comparison, figure 13*c* shows a theoretical simulation produced by computing $|C(x,y)|$ using methods outlined in § 3, scaling the coordinates to conform more closely with the experimental photograph, and shading the resulting contour plot. Figure 14 shows the computed equiphase lines of $C(x,y)$, with the caustic indicated as a chain curve; dislocation points are clearly visible as points where all the equiphase lines meet.

The phase in the integrand of (C 1) has three real stationary points (rays) in the region between the fold curves ('inside' the caustic) and only one outside. This explains why the diffraction

Downloaded from rsta.royalsocietypublishing.org

TABLE 1. POSITIONS OF DISLOCATIONS INSIDE THE CUSP

approximate three-wave formula (C 6)		measured from phase plot (figure 14) (estimated error ±0.05)	
x	y	x	y
−4.34	±0.38	−4.38	±0.38
−5.60	±1.00	−5.56	±1.00
−5.60	±1.66	−5.53	±1.65
−6.63	±0.30	−6.64	±0.30
−6.63	±2.13	−6.47	±2.18
−6.63	±2.74	−6.39	±2.80

pattern is observed to be considerably brighter inside the caustic than outside. The overlapping within the caustic of the two sets of Airy fringes decorating the folds leads to the observed triangular array of bright spots. Dislocations within the caustic occur in pairs. Outside the caustic, $|C|$ decreases away from the main maximum, which is just inside the cusp. Well away from the caustic this decrease is monotonic, but alongside the caustic $|C|$ falls off in an oscillatory manner, as indeed it must to accommodate the row of single dislocations flanking each fold curve.

Since the dislocations are the most delicate features of the pattern, prediction of their positions is a severe test of the stationary phase method, or three-wave theory, applied to (C 1). We begin inside the caustic. The exact stationary phase points are the roots of a cubic equation, which are complicated to write explicitly. Therefore we proceed by perturbation away from the symmetry axis $y = 0$, where the three stationary points are simply $\xi = 0,\ \pm\sqrt{(-x)}$ (real since $x < 0$).

To accomplish this we employ first of all the method of stationary phase, in the form

$$\int_{-\infty}^{\infty} \mathrm{d}\xi\, \mathrm{e}^{\mathrm{i}P(\xi,\boldsymbol{r})} \approx \sum_i \sqrt{\left(\frac{2\pi}{|P''(\xi_i(\boldsymbol{r}),\boldsymbol{r})|}\right)} \exp\left[\mathrm{i}\{P(\xi_i(\boldsymbol{r}),\boldsymbol{r}) + \tfrac{1}{4}\pi \operatorname{sgn} P''(\xi_i(\boldsymbol{r}),\boldsymbol{r})\}\right], \tag{C 3}$$

where $\boldsymbol{r}$ denotes (x, y), primes derivatives with respect to ξ, and $\xi_i(\boldsymbol{r})$ the stationary phase points where $P'(\xi, \boldsymbol{r})$ vanishes. Secondly, we employ the first-order perturbation formula

$$P(\xi_i(\boldsymbol{r}+\delta\boldsymbol{r}), \boldsymbol{r}+\delta\boldsymbol{r}) = P(\xi_i(\boldsymbol{r}),\boldsymbol{r}) + \delta\boldsymbol{r}\cdot[\nabla_{\boldsymbol{r}} P(\xi,\boldsymbol{r})]_{\xi=\xi_i(\boldsymbol{r})} + O(\delta\boldsymbol{r}^2), \tag{C 4}$$

valid for any stationary point ξ_i.

Application of these results to (C 1) with y considered as the perturbation gives

$$C(x,y) \approx \frac{\exp[-\frac{1}{4}\mathrm{i}\pi]}{\sqrt{(-x)}}\{1 + \sqrt{2}\exp[\mathrm{i}(\tfrac{1}{2}\pi - \tfrac{1}{4}x^2)]\cos(y\sqrt{(-x)})\}. \tag{C 5}$$

Dislocation points lie at the zeros of this expression and fall into two classes, with coordinates

$$\left.\begin{aligned} x_m &= -\sqrt{\{(4m-1)\,2\pi\}}, \quad y_{nm} = \{\pm\tfrac{1}{4} + 2n\}\pi/\sqrt{(-x_m)}, \\ \text{and} \qquad x_M &= -\sqrt{\{(4M+1)\,2\pi\}}, \quad y_{NM} = \{\pm\tfrac{1}{4} + (2N+1)\}\pi/\sqrt{(-x_M)}, \end{aligned}\right\} \tag{C 6}$$

where m, M, n, N are integers. Each assignment of m, n or M, N gives a pair of dislocations with the same x value and small y separation, and the pairs are stacked in an alternating sequence. Although this simple perturbation approximation is unaware of the caustic (a failing not possessed by the full stationary phase approximation), the formulae (C 6) give surprisingly accurate predictions of the positions of dislocations within the caustic, as table 1 shows.

This theory shows why dislocations inside the caustic occur in pairs. There are two oblique rays which combine to give the cosine term in (C 5), and these can interfere in two symmetrical

Downloaded from rsta.royalsocietypublishing.org

TABLE 2. POSITIONS OF DISLOCATIONS OUTSIDE THE CUSP

approximate stationary phase (equation C9)		measured from phase plot (figure 14) (estimated error ± 0.05)		exact stationary phase	
x	y	x	y	x	y
−1.58	±1.70	−1.74	±1.65	−1.62	±1.68
−2.98	±3.19	−3.07	±3.13	−2.98	±3.16
−3.97	±4.40	−4.05	±4.35	−3.97	±4.39
−4.79	±5.50	−4.86	±5.45	−4.80	±5.49

ways to give a net amplitude of unity. This resultant then interferes destructively with the third, central, ray to give zeros at the pairs of dislocation points. Obviously, three interfering rays are necessary to produce dislocation pairs.

Finally we study the dislocations outside the caustic. Here there is only one real ray, but the phase in (C 1) has, in addition, two complex stationary points $\xi_i(\boldsymbol{r})$. Analysis of the topography of the integrand shows that only one of these contributes outside the caustic, and its contribution to $C(x, y)$ decays exponentially away from the fold lines. Therefore the single rows of dislocations are produced by two-wave interference of one real ray with one 'complex ray'. Only near the fold line is the complex ray strong enough to cancel the real ray, so it is justified to use perturbation theory again, this time about the fold caustics, on which we denote positions by (x_0, y_0). It suffices to consider only one fold, namely

$$y_0 = +2(-\tfrac{1}{3}x_0)^{\frac{3}{2}}. \tag{C 7}$$

At (x_0, y_0) the stationary phase points are

$$\xi_0 = \begin{cases} +\sqrt{(-\tfrac{1}{3}x_0)}, & \text{(double root)} \\ -2\sqrt{(-\tfrac{1}{3}x_0)}. \end{cases} \tag{C 8}$$

Now let us move off the caustic a small positive distance δ in the x direction; δ is the perturbation being considered. The contribution of the real ray can be found by using the stationary phase formula (C 3) together with the perturbation theory (C 4). The contribution of the complex ray (F. J. Wright, to be published) can be found by using the method of steepest descent (Dingle 1973; Dennery & Krzywicki 1967). These techniques give the following formula for the diffraction wavefunction just outside the caustic:

$$C(x_0+\delta, y_0) \approx \frac{\exp\left[\mathrm{i}\{\tfrac{1}{4}\pi - \tfrac{2}{3}x_0^2 - \tfrac{2}{3}x_0\,\delta\}\right]}{\sqrt{(-3x_0)}} + \frac{\exp\left[\mathrm{i}(\tfrac{1}{12}x_0^2 - \tfrac{1}{6}x_0\,\delta)\right]\exp\left[-\tfrac{2}{9}\sqrt{(x_0\,\delta^3)}\right]}{(-x_0\,\delta)^{\frac{1}{4}}\sqrt{2}}. \tag{C 9}$$

The second term corresponds to the complex ray.

It is not hard to find the zeros of $C(x_0+\delta, y_0)$ numerically from this formula, and, as table 2 shows, the positions of the dislocations agree rather well with those computed exactly. Also shown in table 2 are the dislocations predicted by the exact stationary phase method (F. J. Wright, to be published), i.e. without perturbation theory; evidently this increase in sophistication gives very little improvement.

The results in tables 1 and 2 show that stationary phase methods are remarkably accurate, even when combined with perturbation approximations and even quite near caustics where several stationary points are close together.

Downloaded from rsta.royalsocietypublishing.org

Appendix D. Asymptotic behaviour of dislocation helices

Here we shall justify the statements made in § 5 about the form of the dislocation helices far from the focus and close to the ribs. Rather than trying to approach the straight dislocations of the Pearcey cusp diffraction pattern by moving infinitely far, in physical space, from the focus, we choose another method. Recall that the appearance of the wavelength λ in the scaling factors of (2.7) means that as $\lambda \to 0$ all features of the diffraction pattern flow towards the focus. This means that we can choose a fixed (x', y', z') and then, by letting $\lambda \to 0$, we can allow the pattern to flow past the point and so study the asymptotic behaviour of the dislocation helices close to the ribs.

The windings of these dislocations result from the perturbation of a Pearcey cusp pattern by the locally plane wave associated with the fourth ray contribution to the elliptic umbilic catastrophe. The essential point is that the strength and scale of these two contributions depend differently on λ.

For definiteness we consider only dislocations near the rib with $y' = 0$. Thought of as a function of λ, the plane wave has amplitude of strength $O(1)$ varying on a scale $O(\lambda)$. The cusp pattern has strength $O(\lambda^{-\frac{1}{4}})$ (i.e. its 'singularity index' (Duistermaat 1974; Berry 1976) is $\frac{1}{4}$); its scale in the x' direction (nearly parallel to the symmetry axis of the cusp) is $O(\lambda^{\frac{1}{2}})$ and its scale in the y' direction (transverse to the cusp) is $O(\lambda^{\frac{3}{4}})$ (these results can easily be obtained from the cusp diffraction integral in real space). Near an unperturbed Pearcey dislocation, therefore, the slope of the amplitude in the x' direction is $O(\lambda^{-\frac{1}{4}})/O(\lambda^{\frac{1}{2}}) = O(\lambda^{-\frac{3}{4}})$ while the y' slope is $O(\lambda^{-1})$. This means that the cusp pattern has strength equal to that of the perturbing wave at distances $\delta x'$ and $\delta y'$ from the unperturbed dislocation, where

$$\delta x' = O(\lambda^{\frac{3}{4}}), \quad \delta y' = O(\lambda). \tag{D 1}$$

These are the 'widths' of the helix into which the dislocation is perturbed, that is, the principal axes of its elliptical cross section.

Now we have to convert these widths into the standard coordinates x, y, z of the elliptic umbilic and express them in terms not of λ but of distance s measured in (x, y, z) space along the rib. There is one subtlety. As $\lambda \to 0$ the scaling law (2.7) shows that (since $x' \ll z'$) in transforming from x', y', z' to x, y, z lengths in the x' direction are greatly stretched with respect to those in the z' direction. This has the effect of turning the rib, which is nearly parallel to z' in physical space, so that it becomes asymptotically parallel to x in standard space. The cross-section of the helix in standard space is therefore nearly in the yz plane. If ϕ is the (small) angle between the helix axis and Oz', the section of the helix in the $y'z'$ plane is given by

$$\delta z' = \delta x' \cot\phi = O(\lambda^{\frac{3}{4}}), \quad \delta y' = O(\lambda),$$

remembering that, since the observing point (x', y', z') is fixed, so is ϕ. The scaling law (2.7) then gives for the cross section in the yz plane

$$\delta z = O(\delta z'/\lambda^{\frac{1}{3}}) = O(\lambda^{\frac{3}{4}}/\lambda^{\frac{1}{3}}) = O(\lambda^{\frac{5}{12}}) \tag{D 2}$$

and,

$$\delta y = O(\delta y'/\lambda^{\frac{2}{3}}) = O(\lambda/\lambda^{\frac{2}{3}}) = O(\lambda^{\frac{1}{3}}). \tag{D 3}$$

Since s corresponds to x, (2.7) gives $s = O(\lambda^{-\frac{2}{3}})$, that is

$$\lambda = O(s^{-\frac{3}{2}}). \tag{D 4}$$

Downloaded from rsta.royalsocietypublishing.org

Therefore the helix widths (D 2) and (D 3) become

$$\delta z = O((s^{-\frac{3}{2}})^{\frac{5}{12}}) = O(s^{-\frac{5}{8}}), \quad \delta y = O((s^{-\frac{3}{2}})^{\frac{1}{3}}) = O(s^{-\frac{1}{2}}), \tag{D 5}$$

as stated in § 5.

The number of intersections N' of the dislocation with a plane perpendicular to the axis of the helix in physical space is proportional to the phase change in the perturbing wave across the width $\delta x'$ of the helix. If θ is the (small) angle between the wave normal of the perturbing wave and the rib, this phase change is $\delta x' \sin\theta/\lambda$ and so

$$N' = O\left(\frac{\delta x' \sin\theta}{\lambda}\right) = O\left(\frac{\delta x'}{\lambda}\right) = O(\lambda^{-\frac{1}{4}}),$$

where (D 1) has been used for $\delta x'$, θ being a fixed quantity. Since we wish to have results in xyz space rather than physical space, we require instead the number N of intersections with a plane perpendicular to the helix axis in that space, that is with a yz plane, which corresponds to a $y'z'$ plane. This number N differs from N' by a factor depending only on angles which are constant; the λ dependence is the same. Hence

$$N = O(\lambda^{-\frac{1}{4}}) = O(s^{\frac{3}{8}}),$$

by using (D 4). This formula is the same as that quoted in § 5.

Finally, we estimate the pitch of the helix. In physical space the pitch is $\delta s'$, where, from (5.10c),

$$\delta s' = O(\lambda).$$

In standard space the pitch δs is obtained by again using the fact that the helix axis lies asymptotically nearly parallel to the x axis, so that from (2.7)

$$\delta s = O(\delta s'/\lambda^{\frac{2}{3}}) = O(\lambda^{\frac{1}{3}}) = O(s^{-\frac{1}{2}})$$

by using (D 4), as stated in § 5.

References

Abramowitz, M. & Stegun, I. A. (eds.) 1964 *Handbook of mathematical functions*. New York: Dover.
Airy, G. B. 1838 *Trans. Camb. Phil. Soc.* **6**, 379–402.
Arnol'd, V. I. 1975 *Russ. math. Survs* **30** (5), 1–75.
Berry, M. V. 1976 *Adv. Phys.* **25**, 1–26.
Berry, M. V. & Nye, J. F. 1977 *Nature, Lond.* **267**, 34–36.
Birss, R. R. 1964 *Symmetry and magnetism*. Amsterdam: North-Holland.
Boivin, A., Dow, J. & Wolf, E. 1967 *J. opt. Soc. Am.* **57**, 1171–1175.
Boivin, A. & Wolf, E. 1965 *Phys. Rev.* B **138**, 1561–1565.
Born, M. & Wolf, E. 1975 *Principles of optics*. Oxford: Pergamon Press.
Dennery, P. & Krzywicki, A. 1967 *Mathematics for physicists*. Harper International.
Dingle, R. B. 1973 *Asymptotic expansions: their derivation and interpretation*. London: Academic Press.
Duistermaat, J. J. 1974 *Communs pure appl. Math.* **27**, 207–281.
Green, H. S. & Wolf, E. 1953 *Proc. phys. Soc.* A **66**, 1129–1137.
Hirschfelder, J. O. & Christoph, A. C. 1974 *J. chem. Phys.* **61**, 5435–5455.
Hirschfelder, J. O., Goebel, C. J. & Bruch, L. W. 1974 *J. chem. Phys.* **61**, 5456–5459.
Hirschfelder, J. O. & Tang, K. T. 1976*a* *J. chem. Phys.* **64**, 760–785.
Hirschfelder, J. O. & Tang, K. T. 1976*b* *J. chem. Phys.* **65**, 470–486.
International tables for X-ray crystallography, vol. 1. 1965 Ed. N. F. M. Henry & K. Lonsdale. Birmingham, England: Kynoch Press.
Linfoot, E. H. & Wolf, E. 1956*a* *Proc. Phys. Soc.* B **69**, 823–832.
Linfoot, E. H. & Wolf, E. 1956*b* *Nature, Lond.* **178**, 691–692.
Nye, J. F. 1978 *Proc. R. Soc. Lond.* A **361**, 21–41.
Nye, J. F. & Berry, M. V. 1974 *Proc. R. Soc. Lond.* A **336**, 165–190.

PHILOSOPHICAL TRANSACTIONS OF THE ROYAL SOCIETY A MATHEMATICAL, PHYSICAL & ENGINEERING SCIENCES

PHILOSOPHICAL TRANSACTIONS OF THE ROYAL SOCIETY A MATHEMATICAL, PHYSICAL & ENGINEERING SCIENCES

Downloaded from rsta.royalsocietypublishing.org

Pearcey, T. 1946 *Phil. Mag.* **37**, 311–317.
Poston, T. & Stewart, I. 1978 *Catastrophe theory and its applications*. London: Pitman.
Riess, J. 1970*a* *Ann. Phys.* **57**, 301–321.
Riess, J. 1970*b* *Phys. Rev.* D **2**, 647–653.
Riess, J. 1976 *Phys. Rev.* B **13**, 3862–3869.
Schubnikov, A. V. & Koptsik, V. A. 1974 *Symmetry in science and art*. New York and London: Plenum Press.
Thom, R. 1975 *Structural stability and morphogenesis*. Reading, Mass.: Benjamin.
Trinkaus, H. & Drepper, F. 1977 *J. Phys.* A **10**, L 11–16.
Wolf, E. 1959 *Proc. Phys. Soc.* **74**, 269–280.
Wolf, E. 1960 In *Electromagnetic wave propagation*, pp. 119–125. New York and London: Academic Press.

PHILOSOPHICAL TRANSACTIONS OF THE ROYAL SOCIETY A MATHEMATICAL, PHYSICAL & ENGINEERING SCIENCES

PHILOSOPHICAL TRANSACTIONS OF THE ROYAL SOCIETY A MATHEMATICAL, PHYSICAL & ENGINEERING SCIENCES

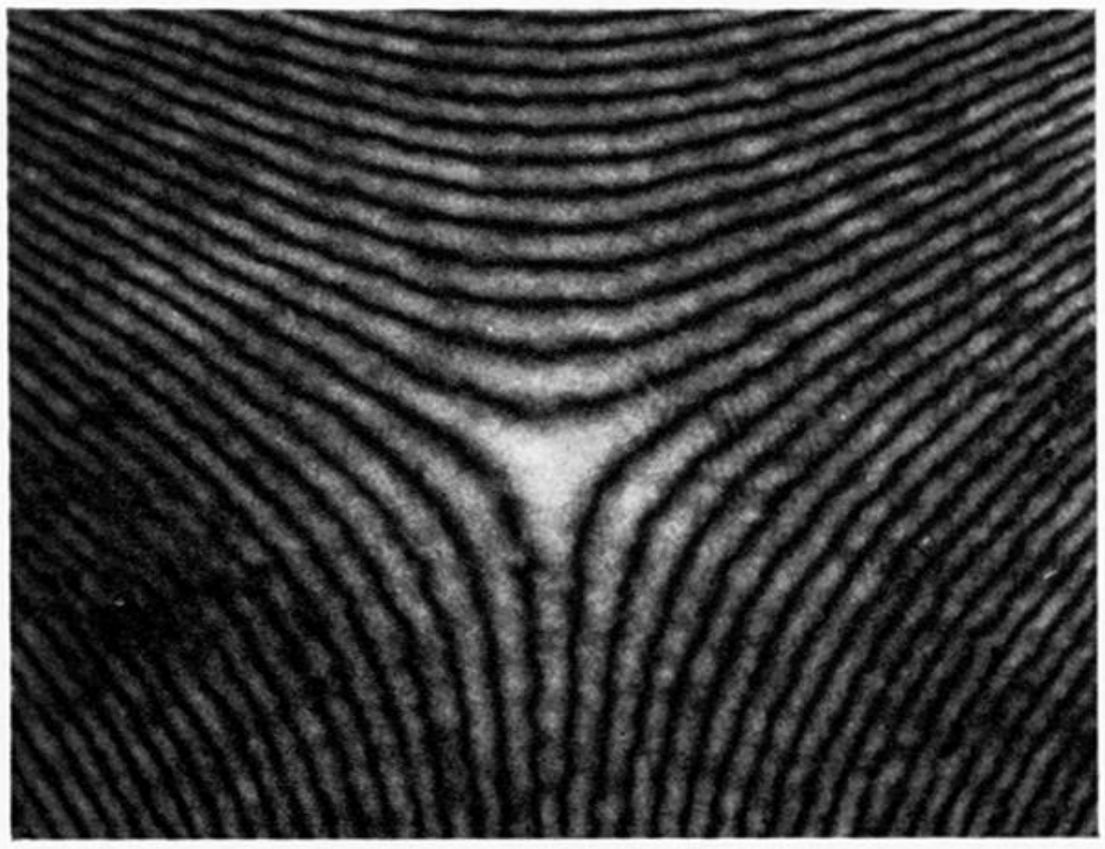

(2*a*)

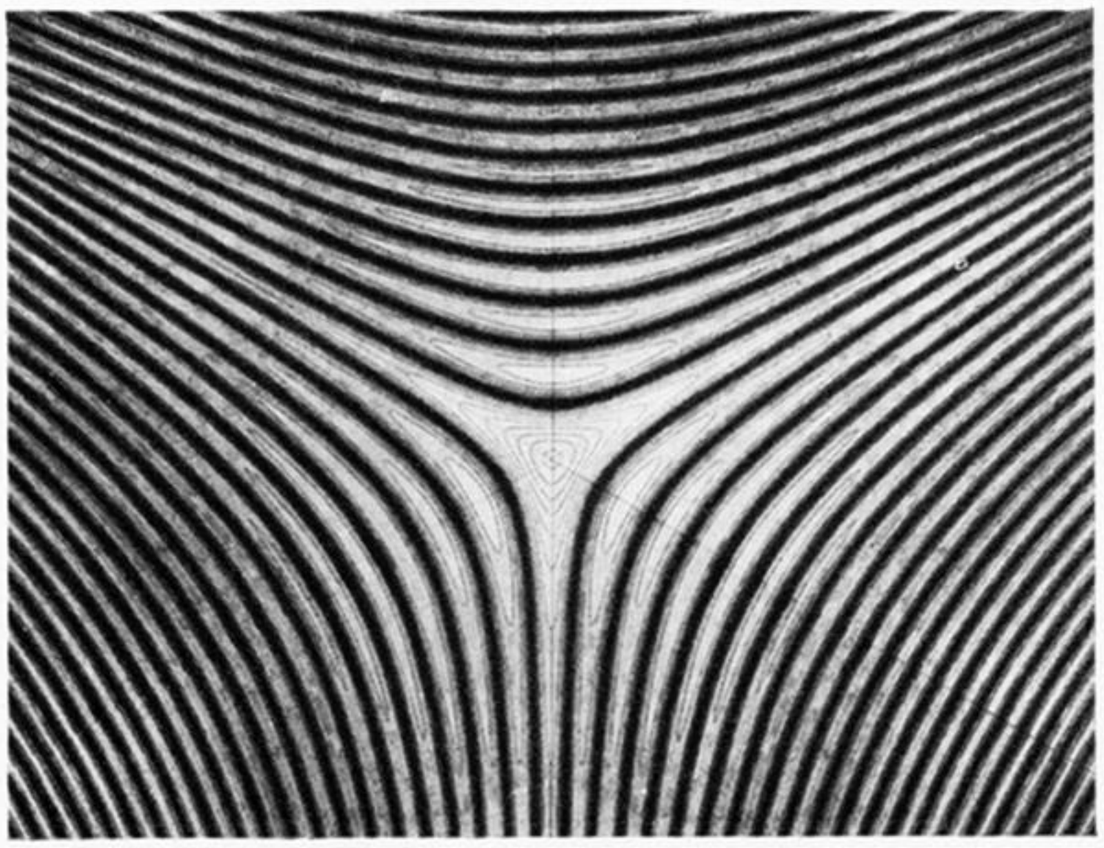

(3*a*)

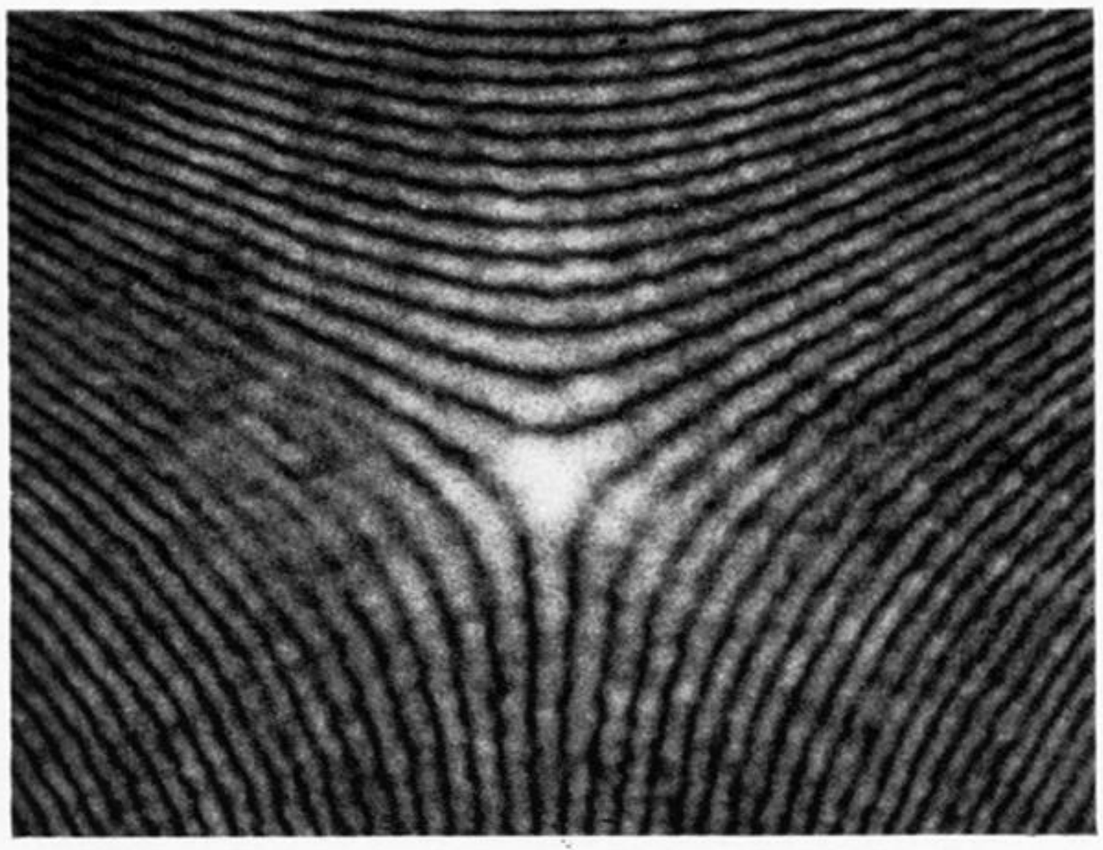

(2*b*)

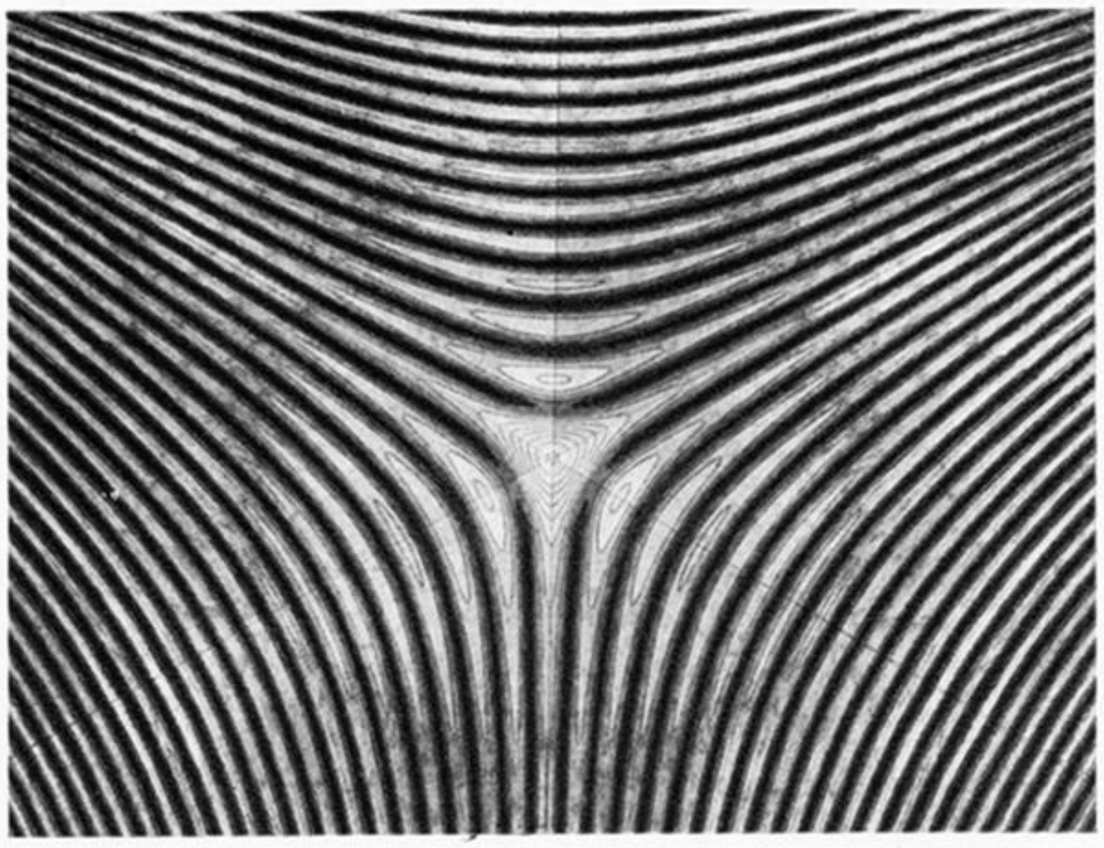

(3*b*)

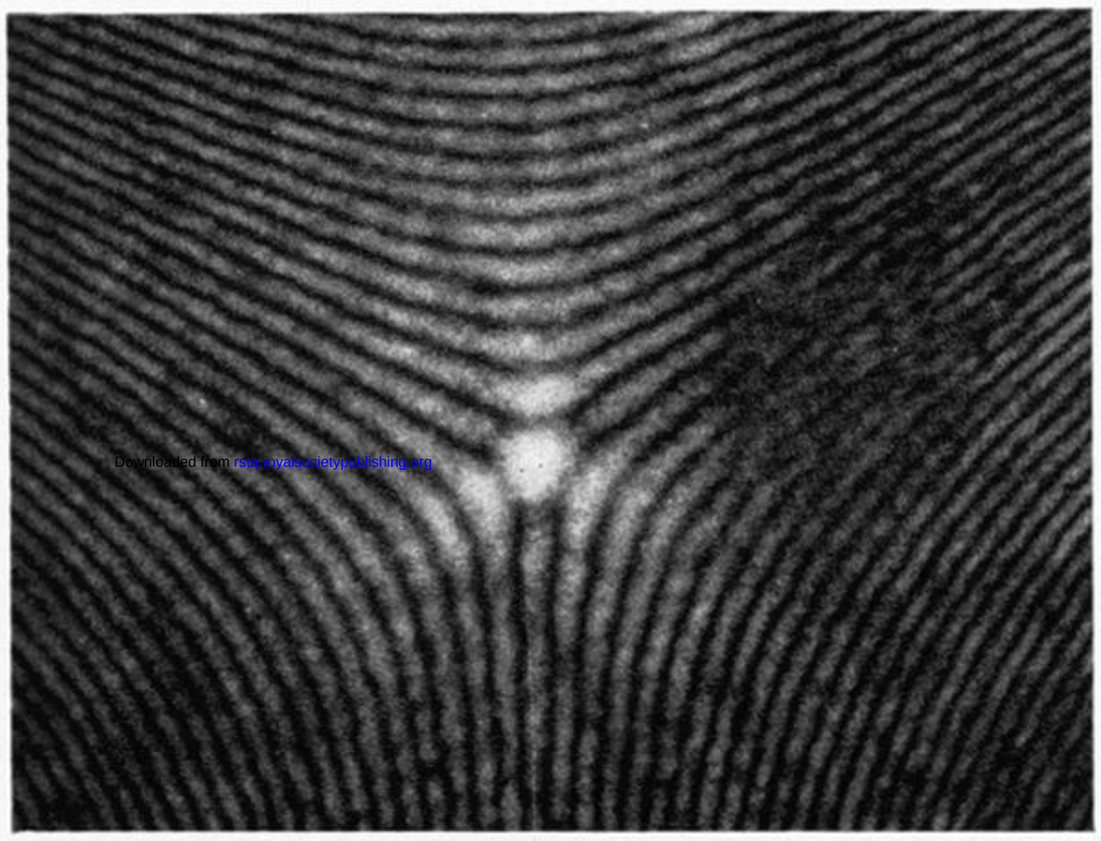

Downloaded from rsta.royalsocietypublishing.org

(2*c*)

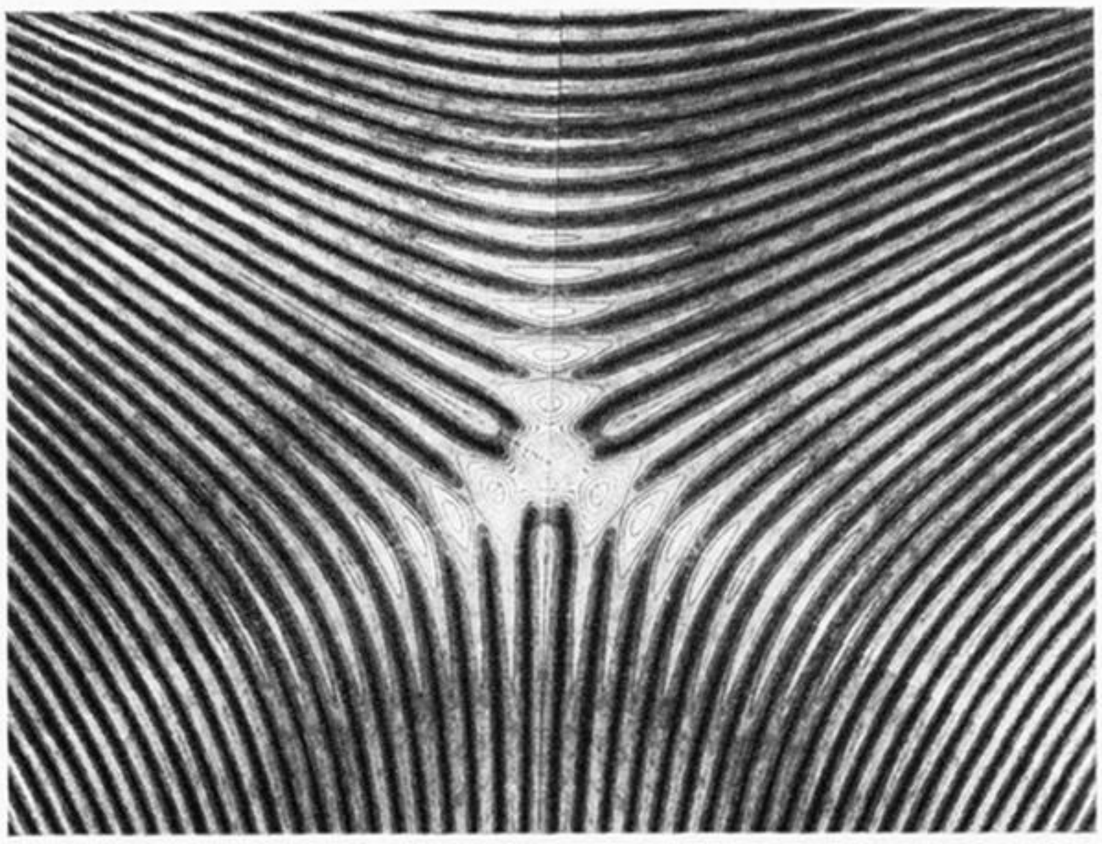

(3*c*)

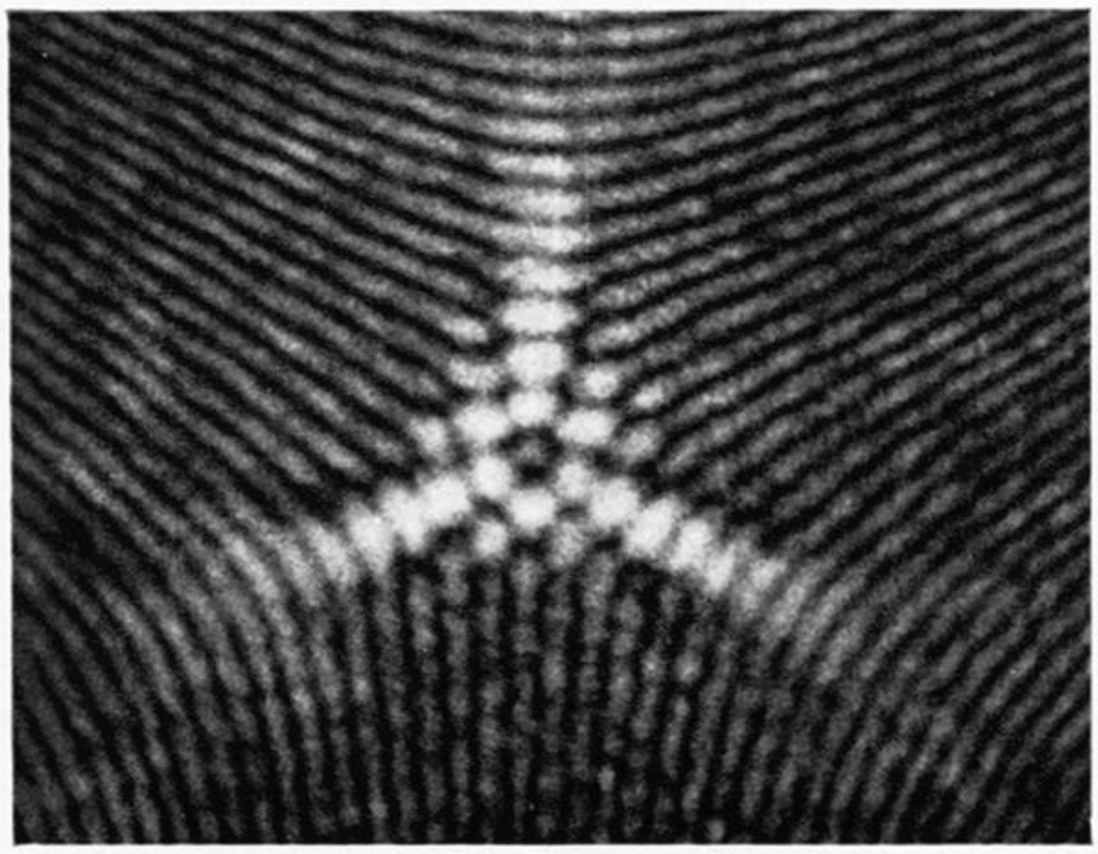

(2*d*)

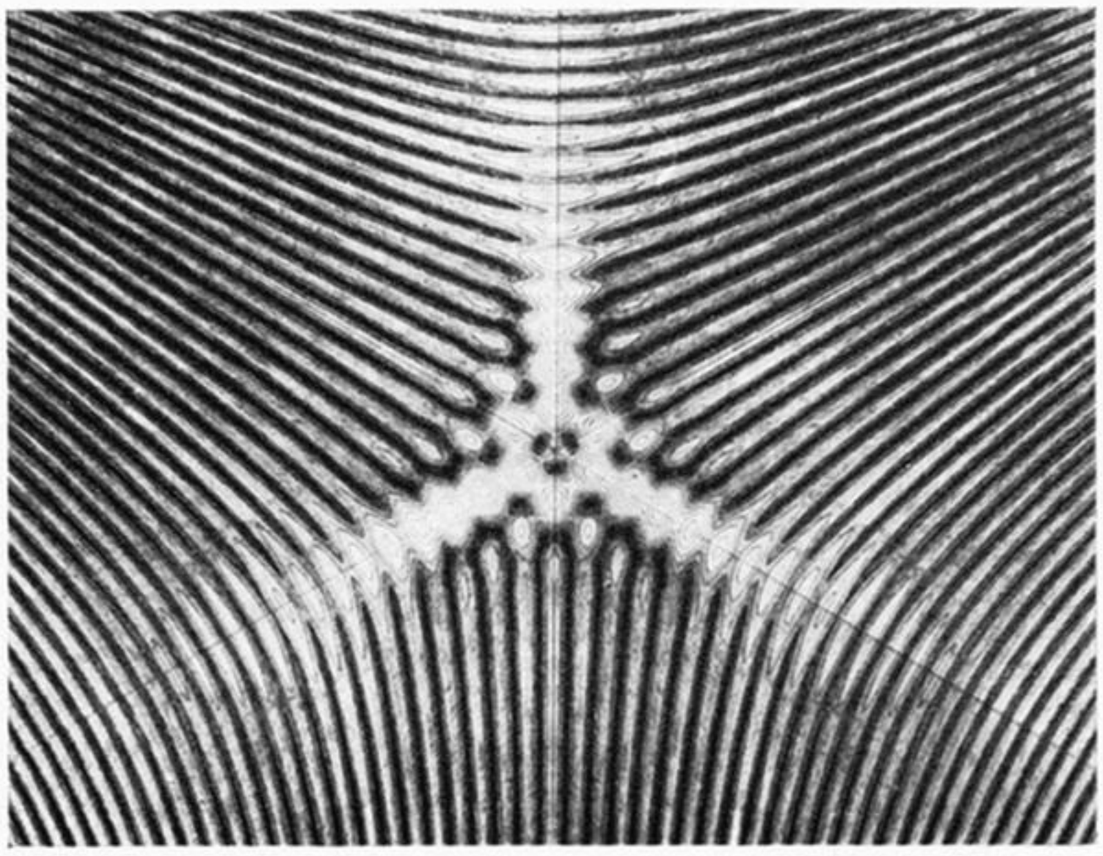

(3*d*)

FIGURES 2*a–d* AND 3*a–d*. For description see plate 3.

PHILOSOPHICAL TRANSACTIONS OF THE ROYAL SOCIETY A MATHEMATICAL, PHYSICAL & ENGINEERING SCIENCES

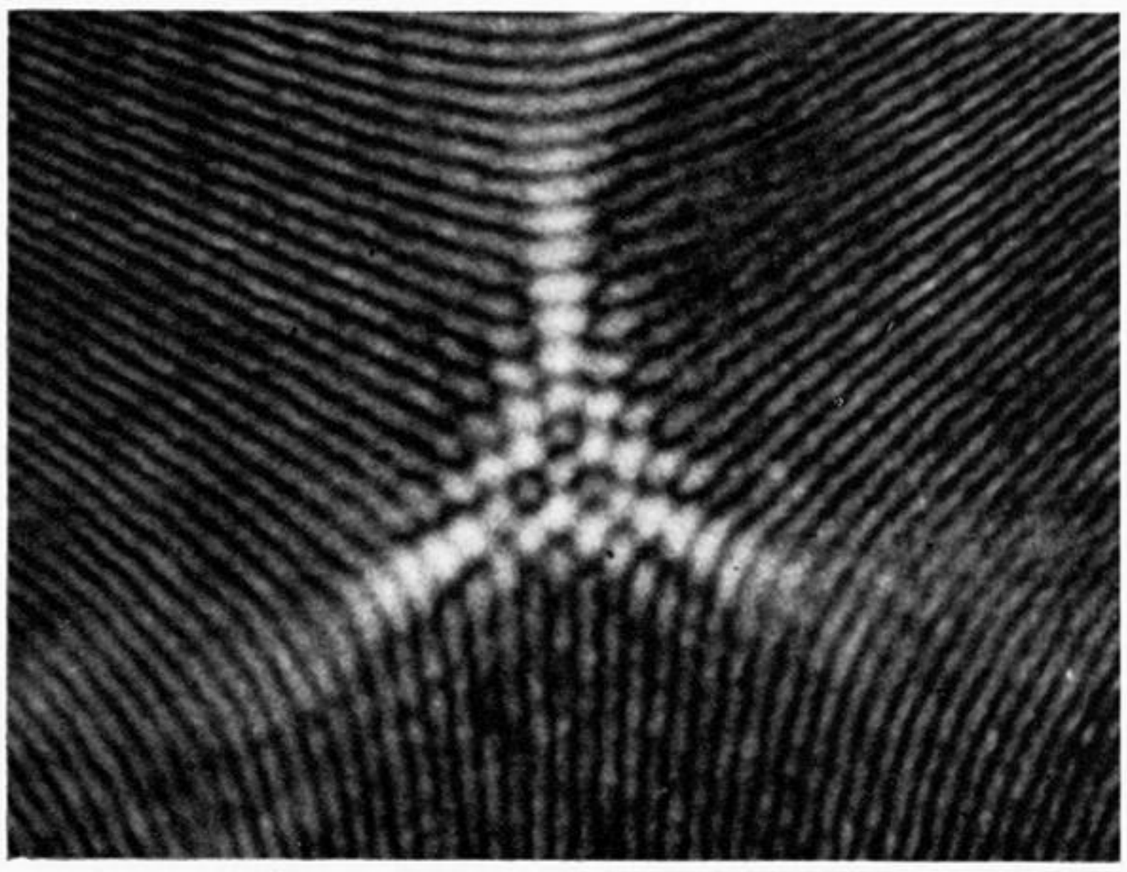

(2e)

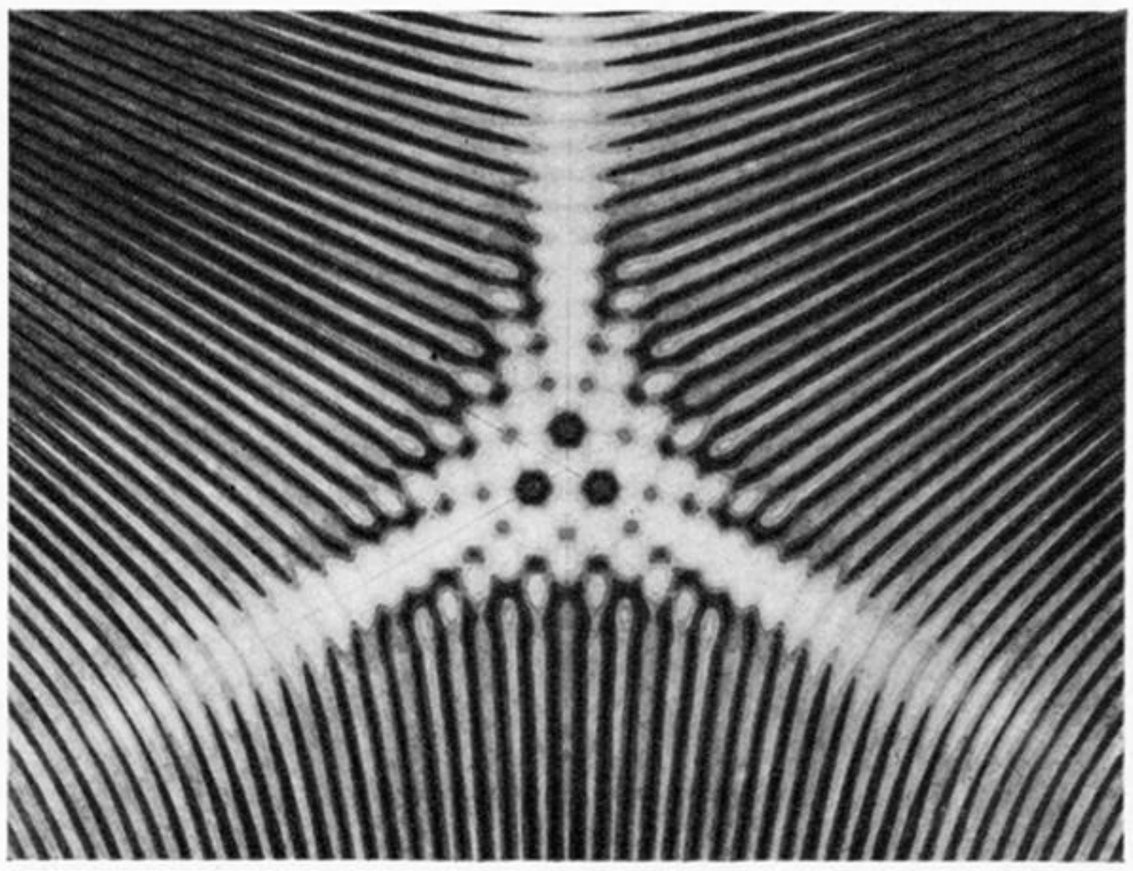

(3e)

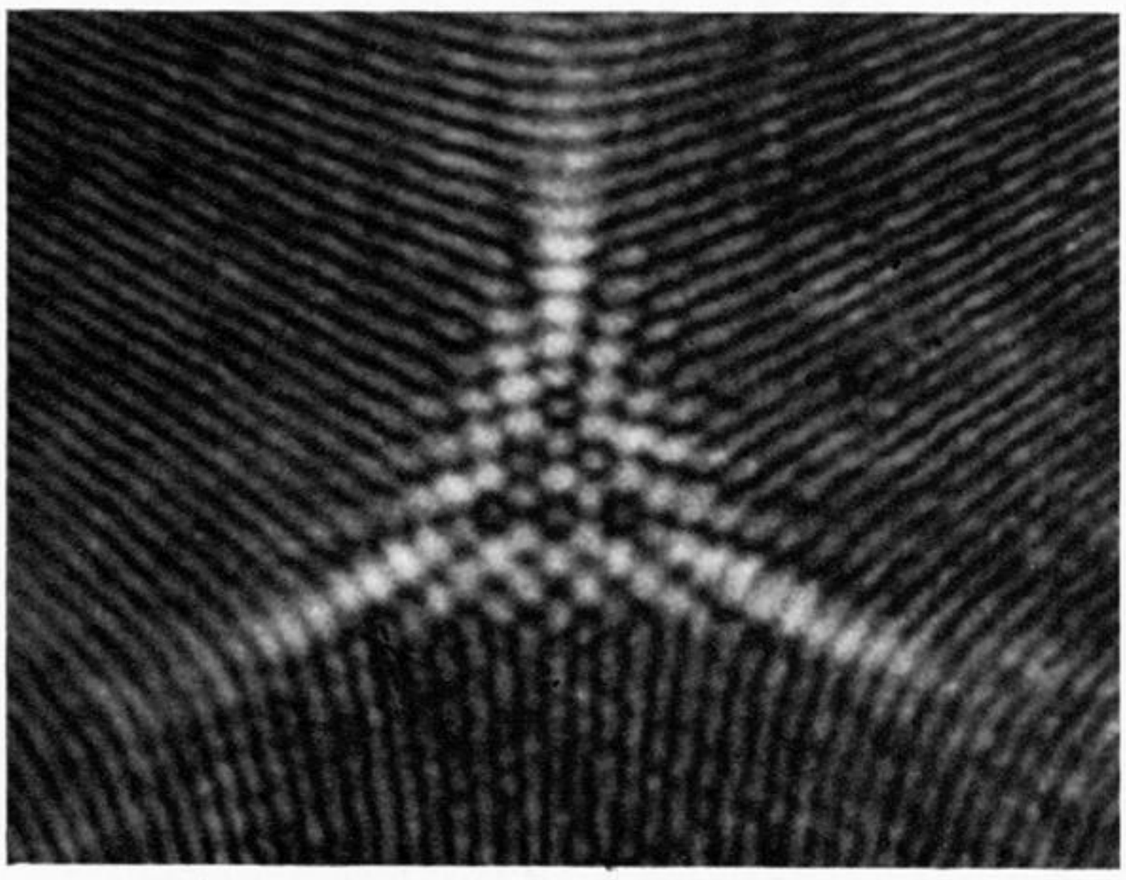

(2f)

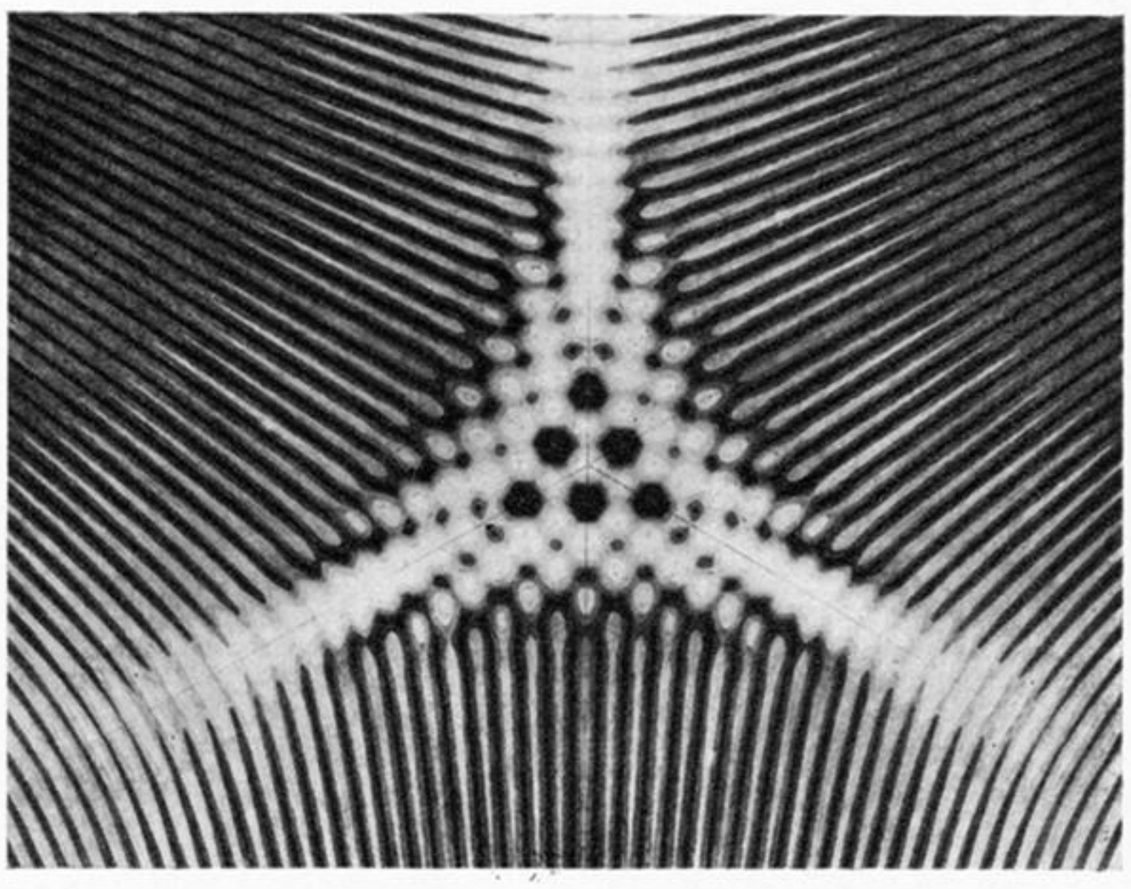

(3f)

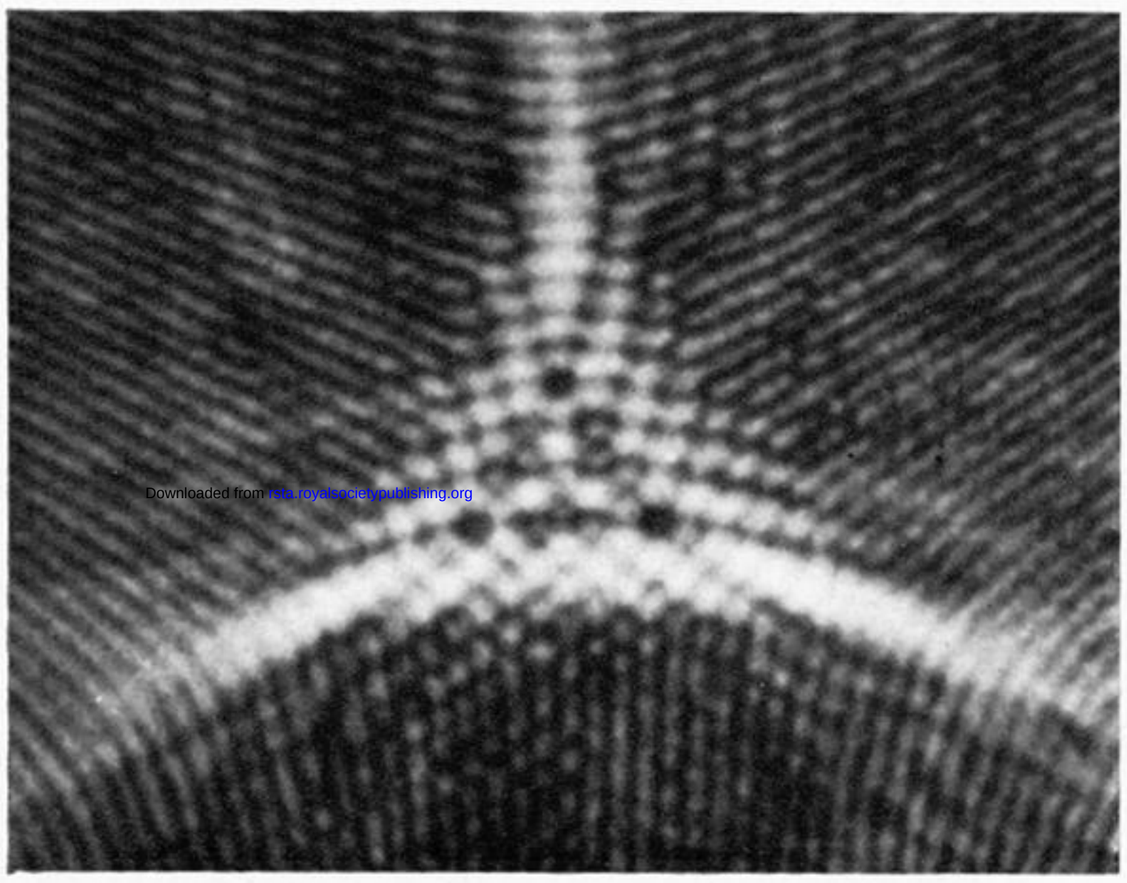

(2g)

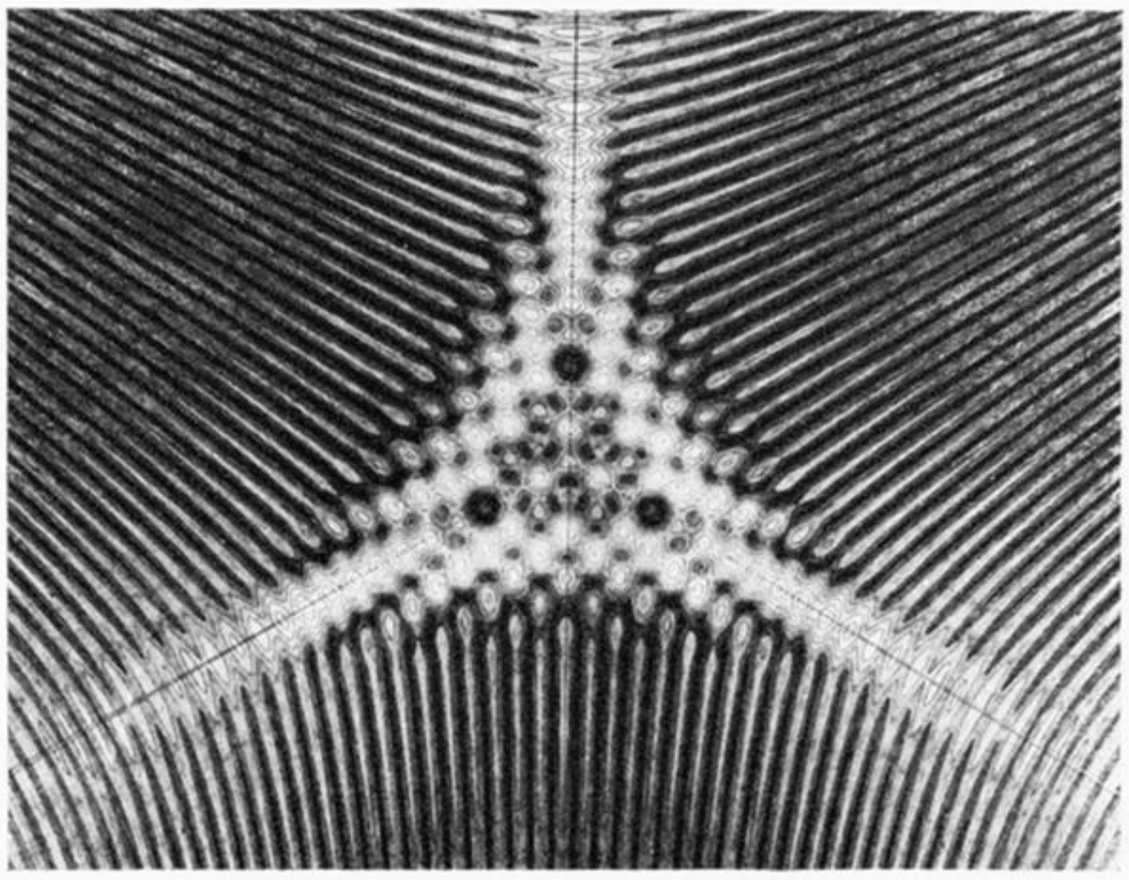

(3g)

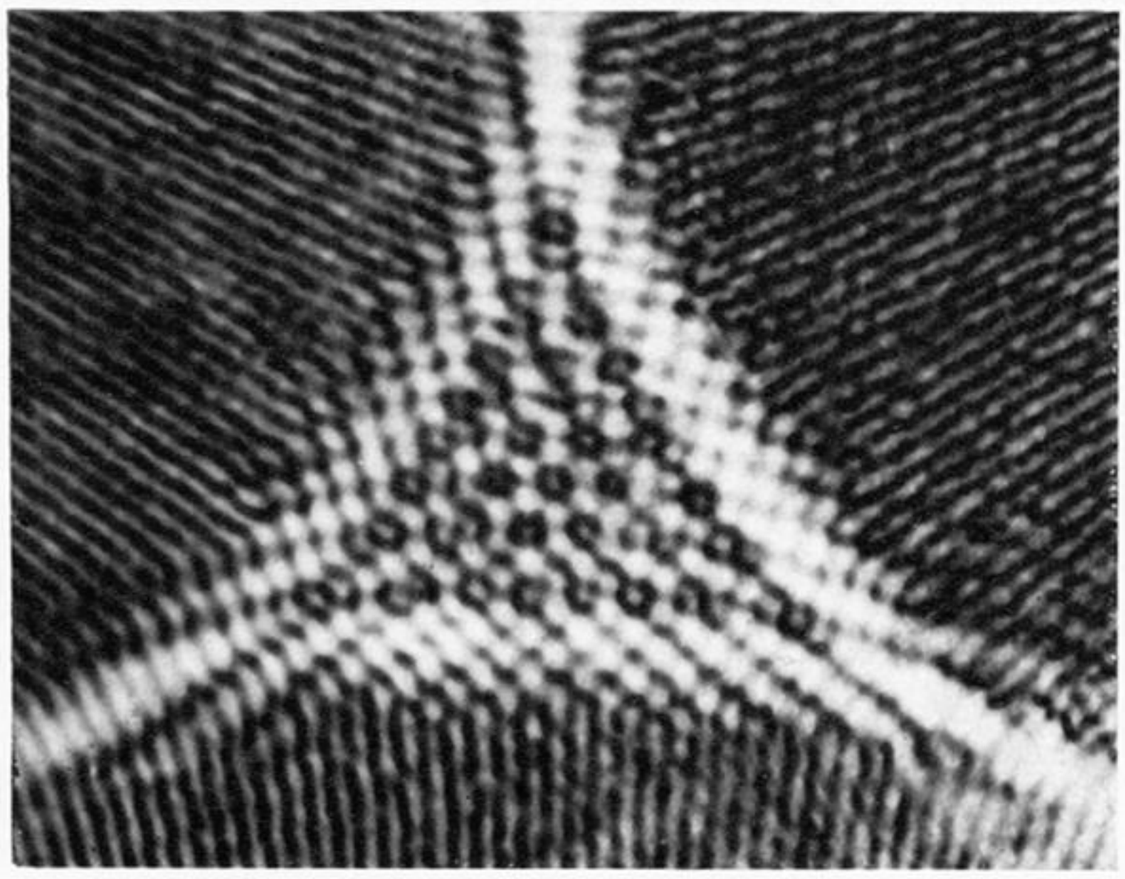

(2h)

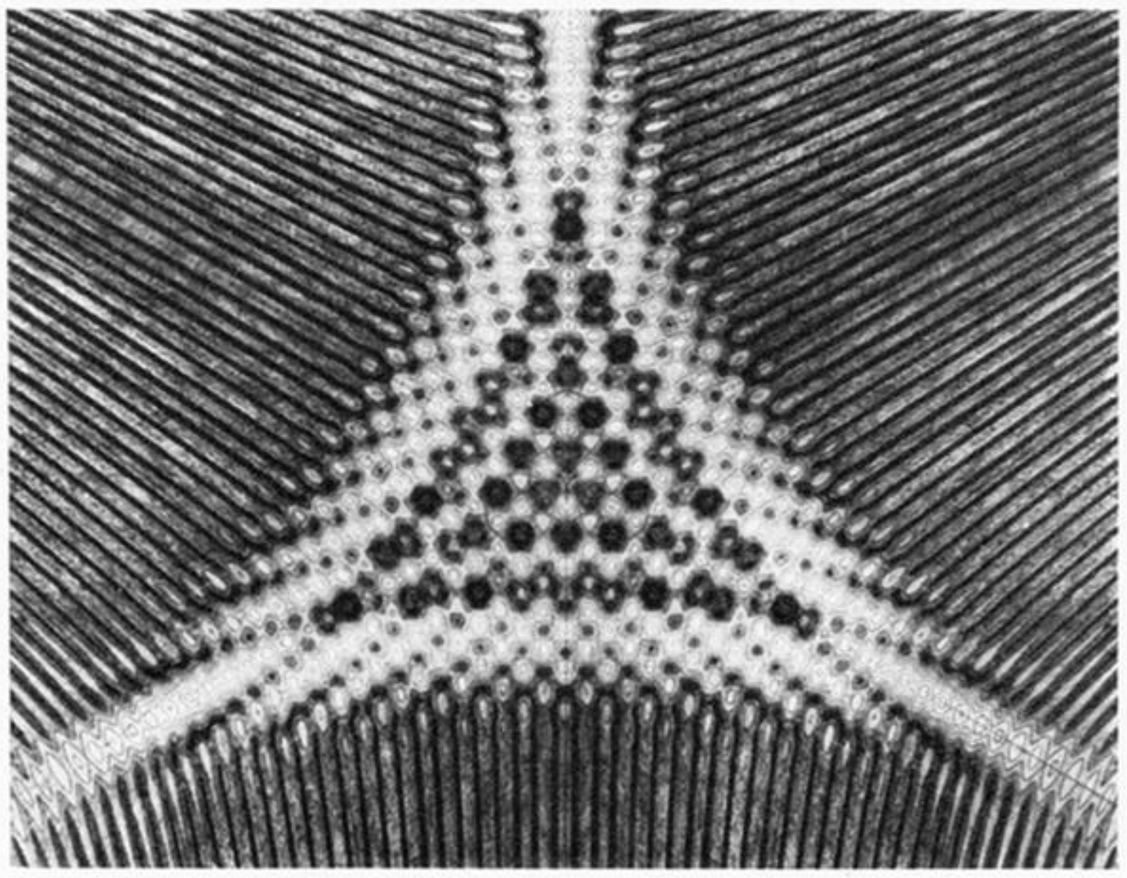

(3h)

FIGURES 2*e–h* AND 3*e–h*. For description see plate 3, opposite.

Downloaded from rsta.royalsocietypublishing.org

PHILOSOPHICAL TRANSACTIONS OF THE ROYAL SOCIETY A MATHEMATICAL, PHYSICAL & ENGINEERING SCIENCES

PHILOSOPHICAL TRANSACTIONS OF THE ROYAL SOCIETY A MATHEMATICAL, PHYSICAL & ENGINEERING SCIENCES

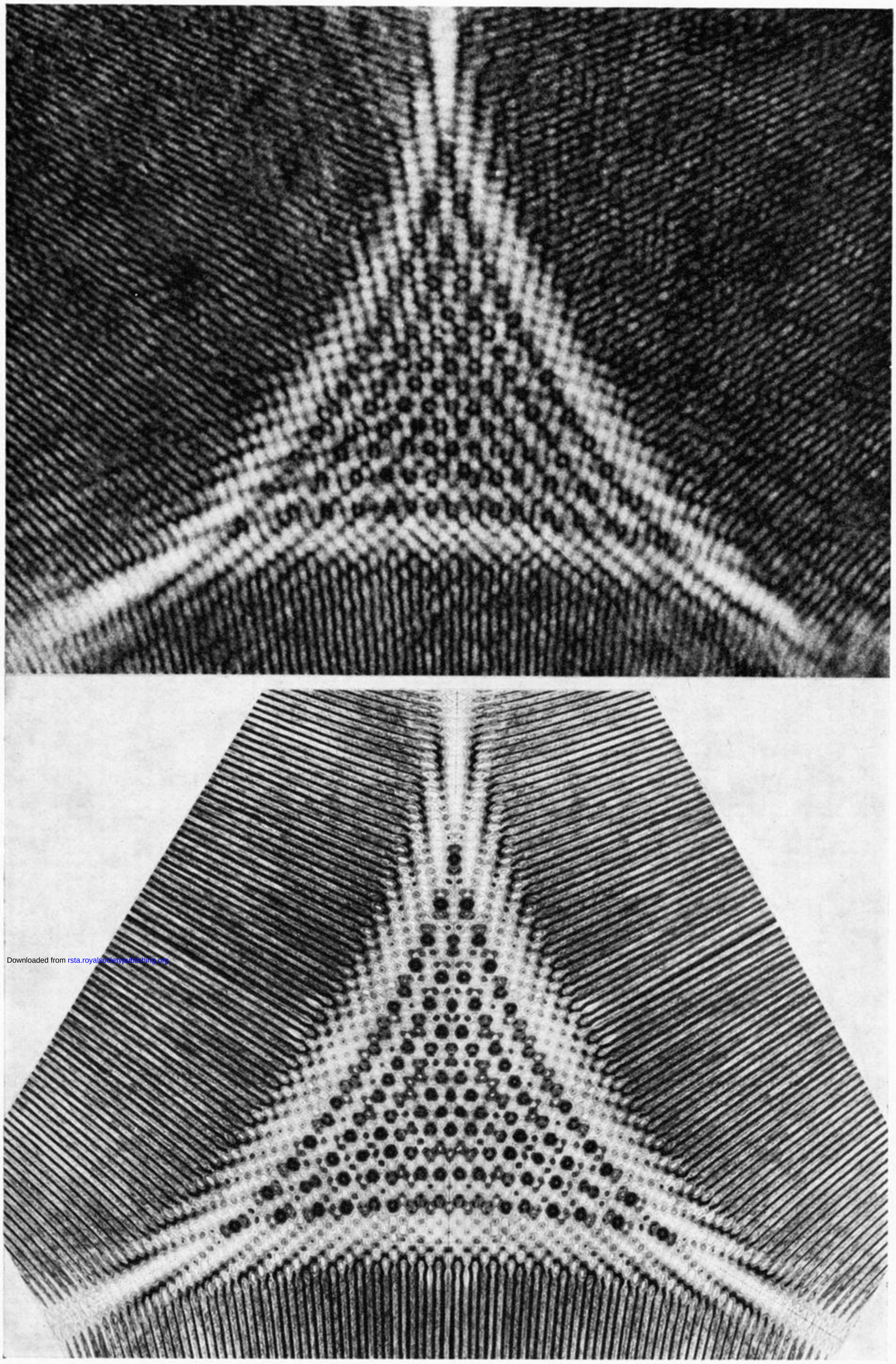

(2*i*)

(3*i*)

Downloaded from rsta.royalsocietypublishing.org

FIGURE 2. Photographs of sections (*a*–*i*) of the elliptic umbilic diffraction catastrophe. Section *a* is through the focus ($z = 0$) and sections *b*–*i* show the unfoldings as z increases. Sections *d*, *e*, *f* show successive triangular numbers (1, 3, 6) of dark hexagons. The x axis points vertically up the page. The length of the side of the caustic triangle in 2*i* is 0.17 mm. z values are (*a*), 0; (*b*), 1; (*c*), 2; (*d*), 3; (*e*), 3.55, (*f*), 3.85; (*g*), 4.0; (*h*), 4.90; (*i*), 5.81.

FIGURE 3. Computer simulations of sections (*a*–*i*) of the elliptic umbilic diffraction catastrophe for comparison with the observations in figure 2. Contour plots of the modulus $|E|$ of the diffraction integral (1.7) at 0.05 intervals were shaded as follows: $0 \leqslant$ black $< 0.05 <$ dark grey $< 0.1 <$ medium dark grey $< 0.15 <$ mid-grey $< 0.2 <$ light grey $< 0.25 <$ white. The x axis points vertically up the page. z values are (*a*), 0; (*b*), 1; (*c*), 2; (*d*), 3; (*e*), 3.55; (*f*), 3. 85; (*g*), 4; (*h*), 5; (*i*), 6.

PHILOSOPHICAL TRANSACTIONS OF THE ROYAL SOCIETY A MATHEMATICAL, PHYSICAL & ENGINEERING SCIENCES

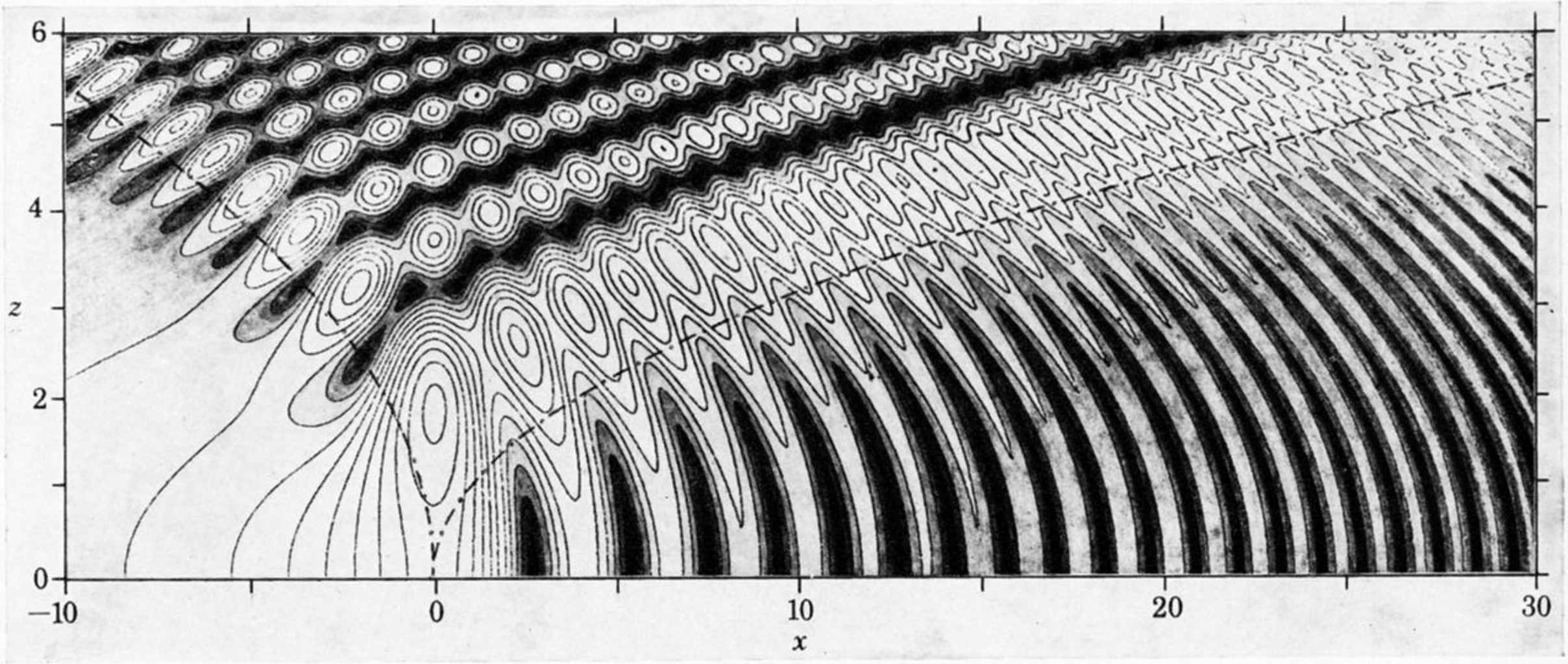

FIGURE 5*a*. For description see opposite.

PHILOSOPHICAL TRANSACTIONS OF THE ROYAL SOCIETY A MATHEMATICAL, PHYSICAL & ENGINEERING SCIENCES

(a)

(b)

(c)

FIGURE 13. For description see opposite.

Downloaded from rsta.royalsocietypublishing.org

PHILOSOPHICAL TRANSACTIONS OF THE ROYAL SOCIETY A MATHEMATICAL, PHYSICAL & ENGINEERING SCIENCES